Downloaded from on November 2, 2026 - Published by Cold Spring Harbor Laboratory Press

Distinct domains of Oligophrenin-1 regulate successive phases of cortical radial migration via RHOA- and PACSIN2-dependent mechanisms

Francesco Boato,[1,4,5] Benjamin de la Cruz Thea,[1,7] Shanu George,[1,7] Yu-Ting Yang,[1] Chia-Lin Wang,[1,6] Sarah Nahlé,[2] Justyna A. Janas,[3] Jean-François Coté,[2] and Linda Van Aelst[1]

[1]Cold Spring Harbor Laboratory, Cold Spring Harbor, New York 11724, USA; [2]Montreal Clinical Research Institute (IRCM), Université de Montréal, Montréal, Quebec H2W 1R7, Canada; [3]Department of Pathology, Institute for Stem Cell Biology and Regenerative Medicine, Stanford University School of Medicine, Stanford, California 94305, USA

Proper assembly of cortical circuits depends on the orderly migration of excitatory projection neurons, a multistep process marked by dynamic cell shape remodeling, including the transition from multipolar-to-bipolar morphology (MP-to-BP) followed by radial glial-guided locomotion. Although molecular players regulating individual stages have been identified, how these steps are coordinated remains unclear. Here, we uncover a critical role for the multidomain Rho-GAP oligophrenin-1 (OPHN1), an X-linked intellectual disability protein, as a dual-function regulator of radial migration. Using a molecular replacement strategy combined with live-cell imaging, we show that OPHN1 governs successive phases of migration through distinct domains and mechanisms: its GAP domain promotes the MP-to-BP transition by suppressing RHOA–ROCK signaling, whereas its second proline-rich domain regulates leading process remodeling and nucleokinesis during locomotion via interaction with the protein kinase C and casein kinase substrate in neurons 2 (PACSIN2). Together, these findings reveal a previously unrecognized role for OPHN1 in early cortical development and demonstrate that its domain-specific functions facilitate stepwise control of radial migration during corticogenesis.

[*Keywords*: Oligophrenin-1; neuronal migration; RHOA signaling; PACSIN2; multipolar-to-bipolar transition; nucleokinesis]

Supplemental material is available for this article.

Received July 23, 2026; revised version accepted September 14, 2026.

The neocortex, a hallmark of the mammalian brain, is characterized by its six-layered architecture and its central role in orchestrating higher-order cognitive and sensorimotor functions (Molyneaux et al. 2007; Greig et al. 2013; Jabaudon 2017). Its construction follows a highly ordered developmental program whose early stages involve the transition of neuroepithelial cells into radial glial progenitors (RGPs) within the dorsal telencephalon. These RGPs serve as the primary source of all cortical excitatory projection neurons, which arise through successive divisions either directly from RGPs in the ventricular zone (VZ) or indirectly via intermediate progenitors in the subventricular zone (SVZ) (Malatesta et al. 2000; Miyata et al. 2001; Noctor et al. 2001; Malatesta and Götz 2013; Taverna et al. 2014). Once generated, the newborn projection neurons undergo a precisely orchestrated migration from their site of birth to the nascent cortical plate (CP), where they settle into distinct laminar positions and differentiate, extending axons and dendrites to establish appropriate synaptic connectivity (Marin and Rubenstein 2003; Kriegstein and Noctor 2004; Casanova and Trippe 2006; Ayala et al. 2007; Valiente and Marín 2010; Cooper 2013; Greig et al. 2013; Silva et al. 2019; Hansen and Hippenmeyer 2020; Vaid and Huttner 2022). This tightly regulated migration is fundamental for establishing functional cortical circuits. It is therefore not surprising that disruptions at any stage of this process have been linked to neurodevelopmental disorders, including intellectual

Present addresses: [4]Children's Hospital Los Angeles, The Saban Research Institute, Los Angeles, CA 90027, USA; [5]Keck School of Medicine of the University of Southern California, Los Angeles, CA 90033, USA; [6]Clinical Laboratory Evaluation Program, Wadsworth Center, New York State Department of Health, Albany, NY 12237, USA.
[7]These authors contributed equally to this work.
Corresponding author: vanaelst@cshl.edu
Article published online ahead of print. Article and pubication date are online at http://www.genesdev.org/cgi/doi/10.1101/gad.354125.126. Freely available online through the *Genes & Development* Open Access option.

© 2026 Boato et al. This article, published in *Genes & Development*, is available under a Creative Commons License (Attribution-NonCommercial 4.0 International), as described at http://creativecommons.org/licenses/by-nc/4.0/.

Downloaded from on November 2, 2026 - Published by Cold Spring Harbor Laboratory Press

disability (ID), autism spectrum disorder, and epilepsy (Ross and Walsh 2001; Métin et al. 2008; Valiente and Marín 2010; Wegiel et al. 2010; Fernández et al. 2016; Stouffer et al. 2016; Francis and Cappello 2021).

To reach their final positions within the CP, cortical projection neurons execute a multistep migratory program composed of distinct migratory modes that evolve as the cortical wall expands. While the earliest-born cortical projection neurons migrate through somal translocation, the later-generated majority rely on radial glia-guided locomotion as the cortical wall thickens (Nadarajah et al. 2001; Noctor et al. 2004). This latter mode of migration involves a series of highly coordinated morphological transformations. Following an initial radial displacement from their birthplace into the SVZ/intermediate zone (IZ), newborn neurons adopt a multipolar morphology, extending multiple dynamic neurites while exhibiting little sustained directional migration. They subsequently undergo a multipolar-to-bipolar (MP-to-BP) transition, acquiring a bipolar shape with distinct leading and trailing processes, which enables radial glia-guided locomotion through the IZ and into the CP. During this phase, neurons extend and stabilize their leading process and migrate via repeated cycles of nucleokinesis, in which the centrosome moves forward into a dilation within the proximal leading process, followed by translocation of the nucleus toward the centrosome. Upon reaching the upper CP and contacting the marginal zone, locomoting neurons detach from the radial glial fibers and undergo terminal translocation to achieve their final laminar positioning (Marin and Rubenstein 2003; Tabata and Nakajima 2003; Ayala et al. 2007; Valiente and Marín 2010; Cooper 2013).

Of the successive phases of radial migration, the MP-to-BP transition and radial glia-guided locomotion represent the most prolonged and complex stages. Given that radial glia-guided locomotion depends on the successful completion of the MP-to-BP transition, these successive steps must be tightly coordinated to ensure proper neuronal positioning and cortical layer formation. Over the past several years, a number of studies have examined the intrinsic mechanisms governing each of these individual phases, revealing distinct molecular and structural components that regulate the dynamic remodeling of the actin and microtubule cytoskeletons, vesicular trafficking, and cell adhesion (Gleeson et al. 1999; Kawauchi et al. 2006; Creppe et al. 2009; Heng et al. 2010; Jossin and Cooper 2011; Kawauchi 2011; Pacary et al. 2011; Shikanai et al. 2011; Godin et al. 2012; Moon and Wynshaw-Boris 2013; Azzarelli et al. 2014; Insolera et al. 2014; Wu et al. 2014; Lian and Sheen 2015; Francis and Cappello 2021; Liaci et al. 2021). Despite these advances, how the MP-to-BP transition and subsequent radial glia-guided locomotion are coordinated at the molecular level remains poorly understood.

Here, we identify oligophrenin-1 (OPHN1) as a previously unrecognized regulator of both the MP-to-BP transition and radial glia-guided locomotion. OPHN1 is a multidomain Rho GTPase-activating protein (Rho-GAP) belonging to the GRAF family (Billuart et al. 1998). In addition to a central GAP domain, it contains an N-terminal Bin/Amphiphysin/Rvs (BAR) domain, a pleckstrin homology (PH) domain, and three C-terminal proline-rich domains (PRDs). Notably, *OPHN1* was the first Rho-related gene identified as causative for a syndromic form of ID. Individuals with *OPHN1* mutations typically present with developmental delay, learning disabilities, behavioral problems, and epileptic seizures, underscoring its important role in normal brain development (Billuart et al. 1998; Tentler et al. 1999; Bergmann et al. 2003; Philip et al. 2003; des Portes et al. 2004; Chabrol et al. 2005; Zanni et al. 2005; Pirozzi et al. 2011; Santos-Rebouças et al. 2014; Moortgat et al. 2018; Schwartz et al. 2019). To date, most studies have focused on OPHN1's functions during postnatal and adult stages, particularly in synapse development and plasticity (Govek et al. 2004; Khelfaoui et al. 2007, 2009, 2014; Nadif Kasri et al. 2009, 2011; Nakano-Kobayashi et al. 2009, 2014; Powell et al. 2012), with a few addressing its role in postnatal/adult neurogenesis (Compagnucci et al. 2016; Redolfi et al. 2016; Allegra et al. 2017). However, its function during early cortical development has remained largely unexplored. Here, we show that OPHN1 is abundantly expressed in the embryonic neocortex and is required for the proper migration of cortical projection neurons, but not for their generation. Using a molecular replacement strategy and live-cell imaging, we demonstrate that OPHN1 governs radial migration by controlling both the MP-to-BP transition and glial-guided locomotion. Importantly, OPHN1 regulates these two steps through distinct domains and mechanisms: its Rho-GAP domain controls the MP-to-BP transition via a RHOA/ROCK-dependent pathway, whereas its second PRD mediates leading process morphogenesis and nucleokinesis, key processes underlying locomotion, through interaction with the adaptor protein PACSIN2. Together, these findings establish OPHN1 as a key regulator of the MP-to-BP transition and radial glia-guided locomotion, providing new insight into how sequential steps of cortical projection neuron migration are coordinated during early brain development and establishing a framework for understanding the developmental role of this ID-associated protein.

Results

OPHN1 is expressed in the developing neocortex

To assess the potential role of OPHN1 in mammalian neocortical development, we examined its expression in the embryonic and early postnatal mouse neocortex. Western blot analysis of neocortical lysates showed weak OPHN1 expression at embryonic day (E) 11, followed by a steady increase from E13 to postnatal day (P)3, corresponding to the peak period of cortical neurogenesis and neuronal migration (Fig. 1A). To determine the spatial expression patterns of OPHN1 in the developing neocortex, we performed immunohistochemistry on coronal brain sections at E16 using antibodies against OPHN1, the neural progenitor marker Nestin, and the early neuronal marker βIII-tubulin (TUJ1). OPHN1 expression was detected in

Downloaded from on November 2, 2026 - Published by Cold Spring Harbor Laboratory Press

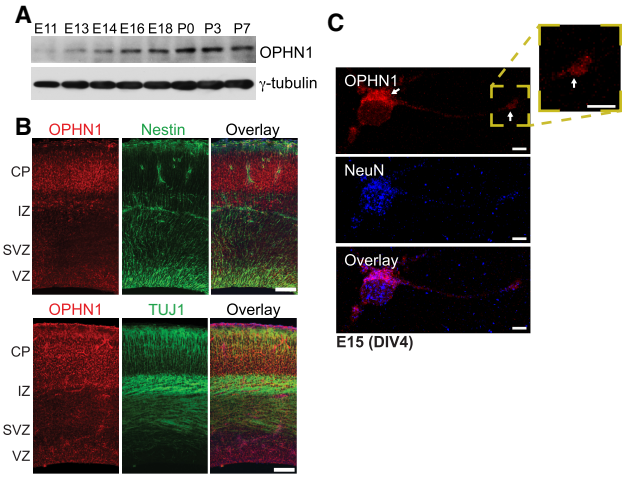


Figure 1. Expression and localization of OPHN1 in the developing mouse cortex. (*A*) Western blot of cortical lysates from E11 to P7 brains probed with antibodies to OPHN1 and γ-tubulin (loading control). (*B*) Coronal sections of E16 mouse neocortex immunostained for OPHN1 and either the neural stem/progenitor marker Nestin or the early neuronal marker βIII-tubulin (TUJ1). (VZ) ventricular zone, (SVZ) subventricular zone, (IZ) intermediate zone, (CP) cortical plate. Scale bars, 50 µm. (*C*) Cultured cortical neurons (DIV4) isolated from E15 neocortices and immunostained for OPHN1 and NeuN (a postmitotic neuronal marker). (*Top right*) An enlarged view of the boxed tip of the neuronal process. Arrows indicate regions of strong OPHN1 immunoreactivity. Scale bars, 5 µm.

Nestin-positive progenitors, particularly within the VZ, and was strong in TUJ1-positive neurons in the IZ and CP (Fig. 1B). To further examine the subcellular distribution of OPHN1 in neurons, we prepared dissociated primary cortical neurons and stained them with antibodies against OPHN1 and NeuN, a marker for postmitotic neurons. In addition to its presence at the tips of neuronal processes, OPHN1 was localized to vesicular structures surrounding the nucleus and was dispersed throughout the cytoplasm (Fig. 1C). Together, these results demonstrate that OPHN1 is prominently expressed in the developing neocortex during peak periods of neurogenesis and neuronal migration.

OPHN1 regulates cortical projection neuron migration in a cell-autonomous manner

Prompted by the observed expression pattern of OPHN1, we next examined its function during embryonic cortical development using an acute loss-of-function approach. We employed RNA interference (RNAi) with vectors encoding two independent, previously validated short hairpin RNAs (shRNAs) targeting *Ophn1* (Ophn1#1 and Ophn1#2) (Nadif Kasri et al. 2009). Each *Ophn1*-targeting or control (scr#1) shRNA vector was coelectroporated with an *EGFP* plasmid into E14 mouse embryonic cortices by in utero electroporation (IUE), and the distribution of EGFP$^+$ cells was analyzed 4 days later at E18 across distinct regions of the developing neocortex. As expected, many EGFP$^+$ cells in the scr#1 shRNA group were located in the upper CP (uCP) (Fig. 2A,B). In contrast, a large fraction of EGFP$^+$ cells in the *Ophn1*#1 and *Ophn1*#2 shRNA groups accumulated in the IZ, with markedly fewer in the uCP (Fig. 2A,B), suggesting that OPHN1-depleted neurons failed to migrate properly through the IZ into the CP. Rescue experiments using an RNAi-resistant *OPHN1-EGFP* cDNA confirmed the specificity of the RNAi effect (Fig. 2A,B).

To determine whether the altered neuronal distribution observed upon OPHN1 depletion was indeed attributable to a migration defect rather than secondary effects on RGP proliferation, scaffold integrity, neuronal production, or laminar fate specification, we performed 5-bromo-2′deoxyuridine (BrdU) incorporation assays, rescue experiments using a Neurod1-driven *OPHN1* cDNA, and analyses of neuronal and layer-specific markers. BrdU incorporation revealed no significant difference in the number of BrdU$^+$ cells between the control and Ophn1#1 or Ophn1#2 shRNA groups (Supplemental Fig. S1A,B), indicating that progenitor proliferation was unaffected. Moreover, coexpression of RNAi-resistant *OPHN1-EGFP* driven by the *Neurod1* promoter, which is active only in postmitotic neurons, rescued the neuronal distribution defect caused by Ophn1#2 shRNA (Fig. 2C,D). Immunostaining with an anti-Nestin antibody further demonstrated that RGP scaffold integrity was preserved following OPHN1 depletion (Supplemental Fig. S1C,D). Neuronal production was also unchanged, as assessed by the proportion of EGFP$^+$ cells expressing TUJ1 (Supplemental Fig. S1E,F), and laminar fate specification was unaffected based on the expression of CUX1 and CTIP2, markers of upper- and deep-layer neurons, respectively (Supplemental Fig. S1G,H). Together, these findings indicate that the aberrant neuronal distribution following OPHN1 depletion results from a migration defect rather than from defects in progenitor proliferation, scaffold integrity, neuronal production, or laminar fate specification.

Next, we investigated whether the migration defect induced by *Ophn1* RNAi persists into postnatal stages. IUEs were performed at E14, and brains were analyzed at P10. In contrast to the scr#1 control, where most EGFP$^+$ cells were located in the upper cortex (uC) as expected, a significant fraction of EGFP$^+$ cells in the OPHN1-depleted group remained in the white matter (WM) and in the lower and middle regions of the cortex (lC and mC) at P10 (Fig. 2E,F), indicating that the defect persists into postnatal stages. Taken together, these results demonstrate a cell-autonomous role for OPHN1 in regulating the migration of projection neurons in the developing neocortex.

OPHN1 is required for bipolar polarization of migrating cortical projection neurons

To gain initial insight into the cellular basis of the migration defect caused by OPHN1 depletion, we performed a more detailed morphological analysis of newborn projection neurons in the IZ and CP at E18 following IUE at E14. Compared to the control scr#1 shRNA and rescue groups, the Ophn1#2 shRNA group showed a marked

Downloaded from on November 2, 2026 - Published by Cold Spring Harbor Laboratory Press

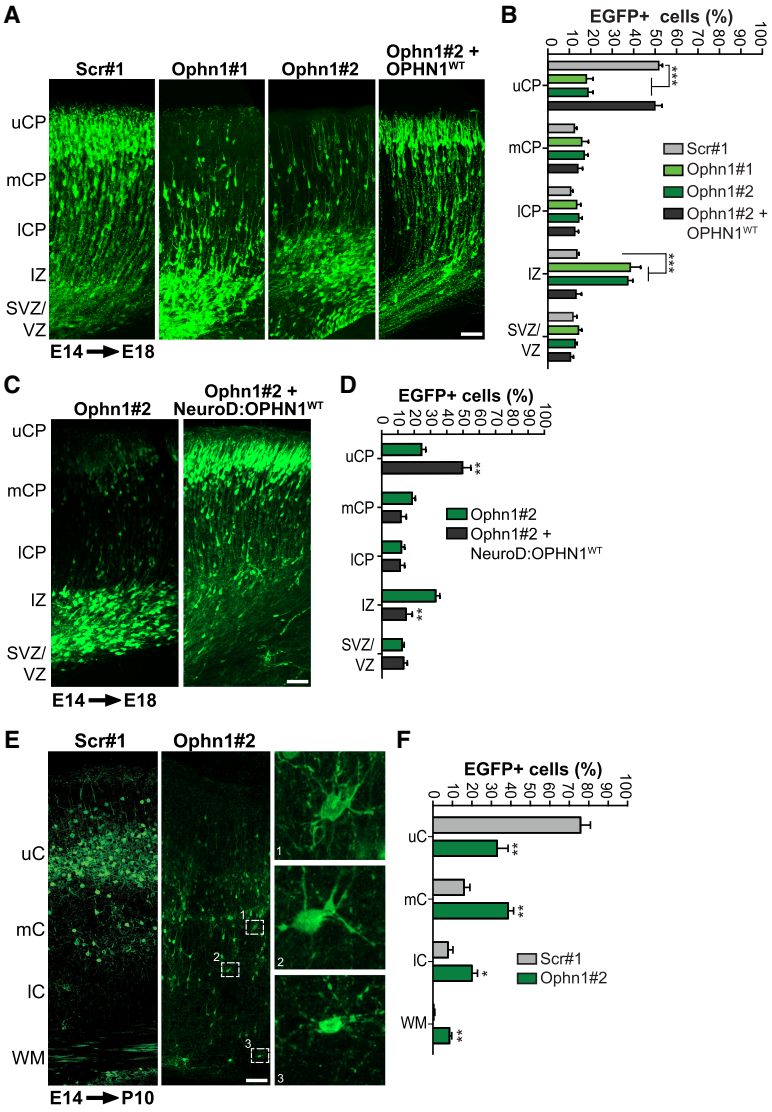


Figure 2. OPHN1 is required cell-autonomously for proper cortical neuronal migration. (*A*,*B*) Knockdown of *Ophn1* impairs radial migration. (*A*) Representative confocal images of E18 neocortices coelectroporated at E14 with an *EGFP*-expressing vector and either a vector expressing nontargeting shRNA (scr#1) or *Ophn1*-targeting shRNA (Ophn1#1 or Ophn1#2), or with Ophn1#2 shRNA and *OPHN1*^{WT}-EGFP, showing the distribution of EGFP$^+$ transfected cells across the VZ, SVZ, IZ, and lower, middle, and upper cortical plate (lCP, mCP, uCP). Scale bar, 50 µm. (*B*) Quantification of the percentage of EGFP$^+$ cells in each region. For quantification, laminar boundaries were defined independently for each brain based on DAPI staining (not shown for clarity) and differences in cell density. Data are presented as mean ± SEM; $n = 3$–4 brains per condition. (***) $P < 0.001$, one-way ANOVA with Dunnett's post hoc test, compared to the scr#1 control. (*C*, *D*) Neuron-specific expression of OPHN1^{WT} rescues the *Ophn1* RNAi-induced migration defect. (*C*) Representative confocal images of E18 neocortices coelectroporated at E14 with an Ophn1#2 shRNA-expressing vector and a vector expressing *EGFP* or *OPHN1*^{WT}*-EGFP* driven by the *Neurod1* promoter (NeuroD:OPHN1^{WT}), showing the distribution of EGFP$^+$ transfected cells across the indicated regions of the developing neocortex. Scale bar, 50 µm. (*D*) Quantification of the percentage of EGFP$^+$ cells in each region. Data are presented as mean ± SEM; $n =$ 3–4 brains per condition. (**) $P < 0.01$, Student's *t*-test. (*E*,*F*) *Ophn1* RNAi-induced migration defect persists into postnatal stages. (*E*) Representative confocal images of P10 neocortices coelectroporated at E14 with an *EGFP*-expressing vector and a vector expressing scr#1 or Ophn1#2 shRNA, showing the distribution of EGFP$^+$ cells across the white matter (WM) and lower, middle and upper cortex (lC, mC, and uC). (*Right* panels) Enlarged views of boxed cells. Scale bar, 50 µm. (*F*) Quantification of the percentage of EGFP$^+$ cells in each region. Data are presented as mean ± SEM; $n = 3$ brains per condition. (*) $P < 0.05$, (**) $P < 0.01$, Student's *t*-test. Unmarked comparisons (vs. control) in *B*, *D*, and *F* are not significant ($P > 0.05$).

increase in the proportion of multipolar (MP) neurons at the expense of bipolar (BP) neurons (Fig. 3A,B). Notably, many neurons that remained in the WM and deep cortical layers at P10 also displayed an MP morphology (Fig. 2E). These findings support a role for OPHN1 in regulating the MP-to-BP transition of migrating cortical projection neurons.

To further examine this, we performed real-time imaging to track the migratory behavior and dynamic cell shape changes of control and OPHN1-depleted neurons. IUEs were performed at E14 to introduce control scr#1 shRNA with *EGFP*, Ophn1#2 shRNA with *EGFP*, or Ophn1#2 shRNA together with RNAi-resistant *OPHN1-EGFP* (rescue), and organotypic cortical slices were prepared at E16. Slices containing sparsely labeled neurons were then subjected to time-lapse imaging over a 13 h period (Fig. 3C). Most neurons in the scr#1 shRNA and rescue groups transitioned from an MP to a BP morphology and migrated efficiently into the CP (Fig. 3C,D; Supplemental Movies S1, S3). In contrast, many neurons in the Ophn1#2 shRNA group failed to undergo this transition and remained largely within the IZ as MP cells throughout the imaging period (Fig. 3C,D; Supplemental Movie S2). Accordingly, their migration velocity was significantly reduced compared to the control groups (Fig. 3E). Together, these results demonstrate that OPHN1 regulates the MP-to-BP transition of newborn cortical projection neurons, a key step that enables their progression through the successive phases of radial migration.

OPHN1 regulates radial migration through GAP-dependent and PRD2-dependent pathways

To probe the molecular mechanisms underlying OPHN1's regulation of cortical projection neuron migration, we began by testing whether its Rho-GAP activity and/or proline-rich domains (PRDs) are required for this function. To this end, we used previously characterized OPHN1 mutants harboring debilitating amino acid

Downloaded from on November 2, 2026 - Published by Cold Spring Harbor Laboratory Press

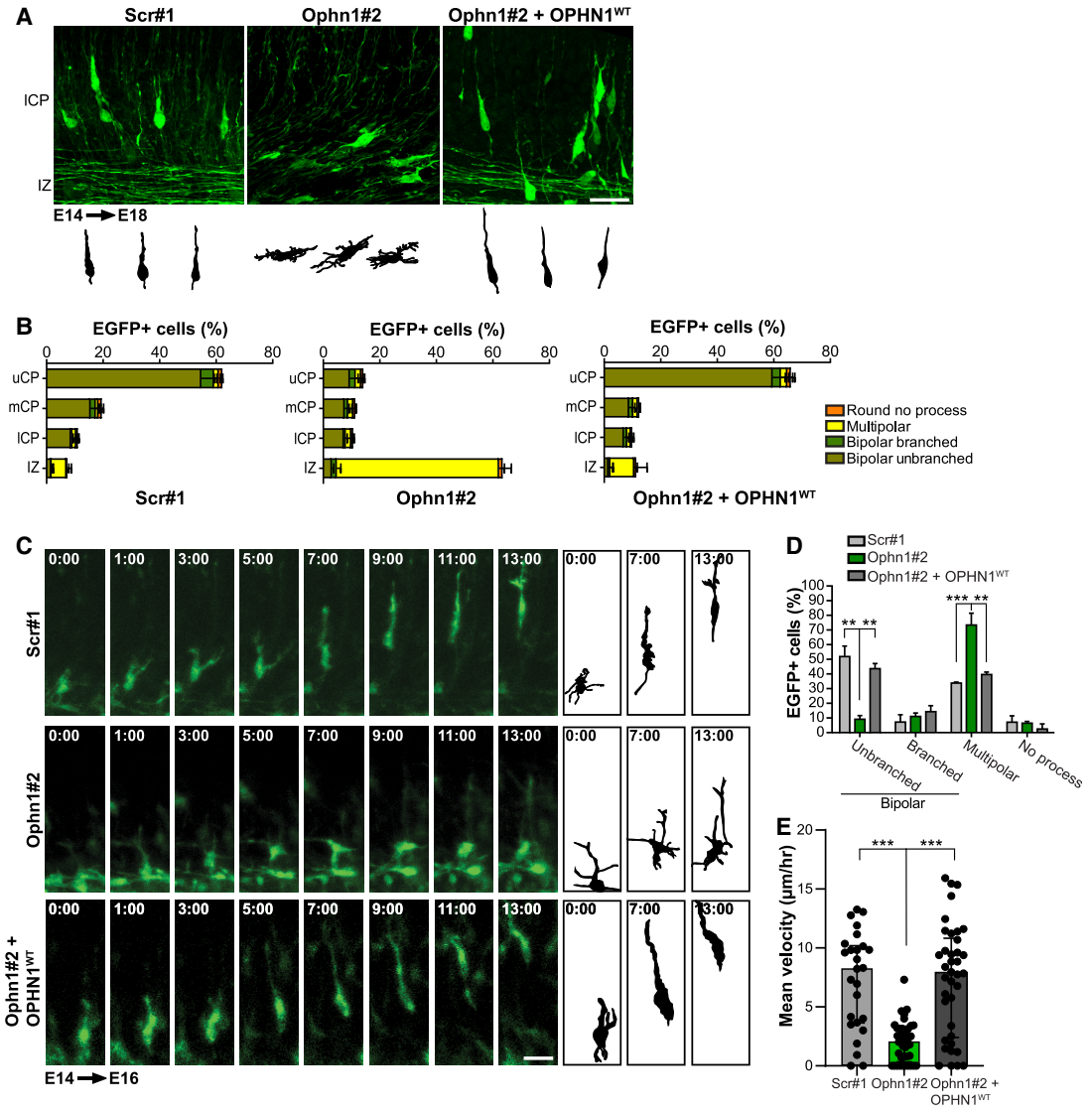


Figure 3. OPHN1 is required for the bipolar polarization of migrating cortical projection neurons. (*A*) Representative high-magnification images and computer-based reconstructions of neurons in the IZ/lCP of E18 neocortices coelectroporated at E14 with vectors expressing scr#1 and *EGFP*, Ophn1#2 shRNA and *EGFP*, or Ophn1#2 shRNA and *OPHN1*^{WT}*-EGFP*. Scale bar, 50 µm. (*B*) Percentage of EGFP$^+$ cells exhibiting bipolar morphology with an unbranched or branched leading process, multipolar morphology, or round morphology lacking processes in the indicated regions of the developing neocortex. $n = 6$ brains per condition. (*C*) Time-lapse images acquired over a 13 h period, taken 2 days after E14 coelectroporation with indicated constructs, showing representative transfected neurons as they exit the IZ and enter the CP. Scale bar, 20 µm. (*Right* panels) Computer-based reconstructions of migrating neurons at the start of the recording and at 7 and 13 h. (*D*) Quantification of the percentage of migrating EGFP$^+$ neurons exhibiting the indicated morphologies within the IZ and CP. Data are presented as mean ± SEM; $n = 26$–41 cells per condition pooled from three independent IUEs. (**) $P < 0.01$, (***) $P < 0.001$, one-way ANOVA with Tukey–Kramer post hoc test. (*E*) Quantification of mean migration velocity. Data are presented as median (IQR); $n = 26$–41 cells per condition pooled from three independent IUEs. (***) $P < 0.001$, Kruskal–Wallis with Dunn's post hoc test.

substitutions in the Rho-GAP domain (GAP*) or in the first (PRD1*), second (PRD2*), or third (PRD3*) PRD (Fig. 4A; Nakano-Kobayashi et al. 2009; Nadif Kasri et al. 2011). Each mutant, fused to EGFP, was cointroduced with Ophn1#2 shRNA into E14 mouse cortices, and their ability to rescue the *Ophn1* RNAi-induced migration defect was assessed 4 days after IUE. While OPHN1^{PRD1*} and OPHN1^{PRD3*} were able to rescue the migration defect caused by OPHN1 depletion, OPHN1^{GAP*} and OPHN1^{PRD2*} were not (Fig. 4B,C). Notably, the defects observed in OPHN1^{GAP*}- and OPHN1^{PRD2*}-expressing neurons were distinct. A large fraction of OPHN1^{GAP*}-expressing neurons remained in the IZ and retained an MP morphology resembling that of OPHN1-depleted neurons (Fig. 4B–E). In contrast, many OPHN1^{PRD2*}-expressing neurons were located beyond the IZ and exhibited a BP morphology; however, a substantial fraction remained stalled in the lower CP (lCP) and middle CP (mCP) and

Downloaded from on November 2, 2026 - Published by Cold Spring Harbor Laboratory Press

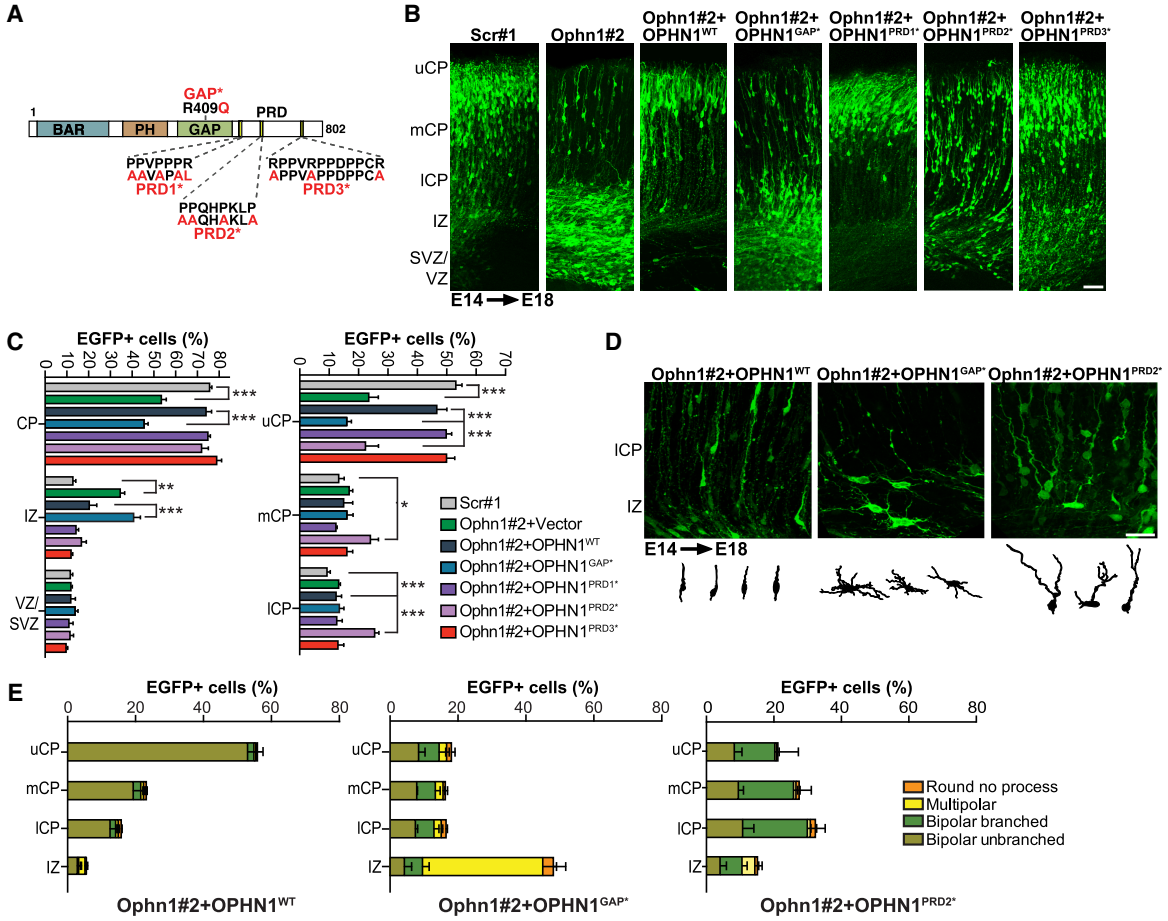


Figure 4. OPHN1 regulates radial migration via GAP-dependent and PRD2-dependent mechanisms. (*A*) Domain structure and point-mutated constructs of *OPHN1*. (*B*) Representative confocal images of E18 neocortices electroporated at E14 with vectors expressing scr#1 shRNA and *EGFP* or Ophn1#2 shRNA together with *EGFP*, $OPHN1^{WT}$-*EGFP*, $OPHN1^{GAP*}$-*EGFP*, $OPHN1^{PRD1*}$-*EGFP*, $OPHN1^{PRD2*}$-*EGFP*, or $OPHN1^{PRD3*}$-*EGFP*, showing the distribution of $EGFP^+$ transfected cells across the indicated regions of the developing neocortex. Scale bar, 50 µm. (*C*) Quantification of the percentage of $EGFP^+$ cells in each region. Data are presented as mean ± SEM; $n = 3–6$ brains per condition. (*) $P < 0.05$, (**) $P < 0.01$, (***) $P < 0.001$, one-way ANOVA with Tukey–Kramer post hoc test. Only selected post hoc comparisons are shown. (*D*) Representative high-magnification images and computer-based reconstructions of neurons in the IZ/lCP of E18 neocortices coelectroporated at E14 with vectors expressing Ophn1#2 shRNA together with $OPHN1^{WT}$-*EGFP*, $OPHN1^{GAP*}$-*EGFP*, or $OPHN1^{PRD2*}$-*EGFP*. Scale bar, 50 µm. (*E*) Percentage of $EGFP^+$ cells exhibiting bipolar morphology with an unbranched or branched leading process, multipolar morphology, or round morphology lacking processes in the indicated regions of the developing neocortex. Data are mean ± SEM. $n = 4$ brains for each condition.

displayed an aberrantly branched leading process and impaired attachment to radial glial fibers (Fig. 4B–E; Supplemental Fig. S2A,B). The defects observed in both $OPHN1^{GAP*}$- and $OPHN1^{PRD2*}$-expressing neurons persisted into postnatal stages (Supplemental Fig. S3A,B).

To further examine these defects and visualize their migratory dynamics, we performed live imaging during the MP-to-BP transition and locomotion phases (Fig. 5A). Consistent with our observations in fixed tissue, $OPHN1^{GAP*}$-expressing neurons largely failed to undergo the MP-to-BP transition and remained in the IZ with an MP morphology throughout the 13 h imaging period (Fig. 5B,C; Supplemental Movie S4). Accordingly, their migration velocity was substantially reduced (Fig. 5D). Most $OPHN1^{PRD2*}$-expressing neurons, on the other hand, transitioned from an MP to a BP morphology and traversed the IZ, but largely stalled in the CP during the locomotion phase, exhibiting extensive leading process branching (Fig. 5B–D; Supplemental Movie S5). Given that forward migration of locomoting neurons relies on repetitive cycles of nucleokinesis, during which the centrosome first advances into a dilation within the leading process followed by nuclear translocation, we next assessed whether this process was also affected. While control $OPHN1^{WT}$-expressing (rescue) neurons typically underwent two to three nucleokinesis events, $OPHN1^{PRD2*}$-expressing neurons exhibited a marked reduction, with the majority undergoing zero to one event over the 13 h imaging period (Fig. 5E). To further confirm defective nucleokinesis, we analyzed the movements of the centrosome and the cell soma. To label the centrosome, we cointroduced a plasmid expressing *Centrin-1*

Downloaded from on November 2, 2026 - Published by Cold Spring Harbor Laboratory Press

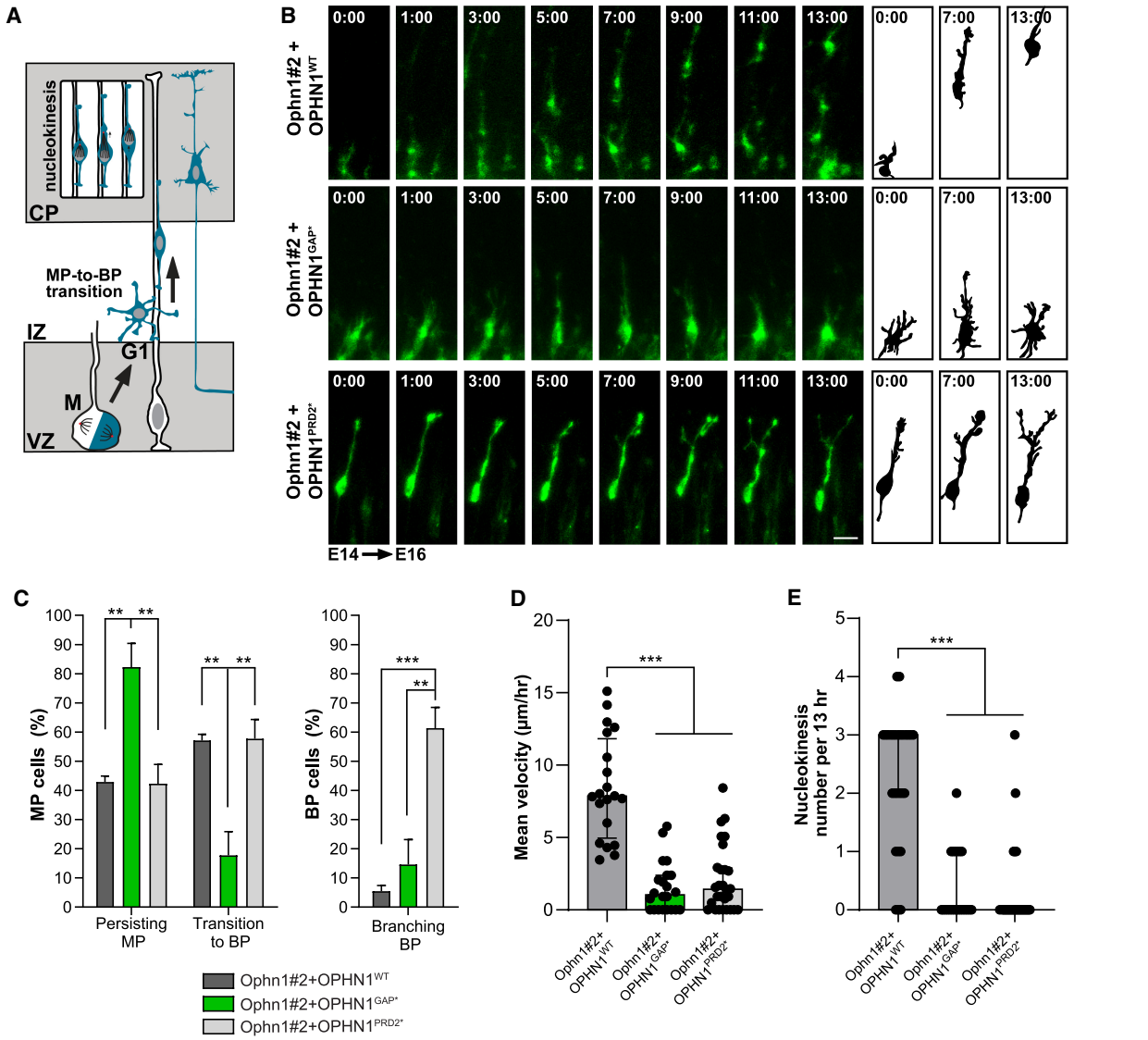


Figure 5. OPHN1 GAP and PRD2 domains control the MP-to-BP transition and locomotion phases, respectively. (*A*) Schematic of the sequential steps of neuronal migration in the embryonic neocortex. (*B*) Time-lapse images acquired over a 13 h period, taken 2 days after E14 coelectroporation with vectors expressing Ophn1#2 shRNA and either *OPHN1^{WT}-EGFP*, *OPHN1^{GAP*}-EGFP*, or *OPHN1^{PRD2*}-EGFP*, showing representative transfected neurons as they exit the IZ and enter the CP. (*Right* panels) Computer-based reconstructions of migrating neurons at the start of the recording and at 7 and 13 h. Scale bar, 20 µm. (*C*) Quantification of the percentage of EGFP$^+$ neurons that remained multipolar (MP) or transitioned to a bipolar (BP) morphology, and of BP neurons exhibiting a branched leading process during the 13 h recording period. Data are presented as mean ± SEM; $n = 20–28$ cells per condition pooled from four independent IUEs. (**) $P < 0.01$, (***) $P < 0.001$, one-way ANOVA with Tukey–Kramer post hoc test. (*D*,*E*) Quantifications of mean migration velocity (*D*) and number of nucleokinesis events per 13 h (*E*). Data are presented as median (IQR); $n = 20–28$ cells per condition pooled from four independent IUEs. (***) $P < 0.001$, Kruskal–Wallis with Dunn's post hoc test.

fused to DsRed-Express along with vectors expressing Ophn1#2 shRNA and either *OPHN1^{WT}-EGFP* or *OPHN1^{PRD2*}-EGFP*. In contrast to control OPHN1^{WT}-expressing neurons, which showed progressive advancement of the centrosome into the leading process in tight coordination with nuclear translocation, OPHN1^{PRD2*}-expressing neurons exhibited minimal movement of both the centrosome and nucleus/soma, remaining mostly stationary during the 13 h imaging period (Supplemental Fig. S4A–C), consistent with a defect in nucleokinesis.

Taken together, our molecular replacement strategy enabled the identification of a dual role for OPHN1 in neuronal migration: regulating the MP-to-BP transition via a GAP-dependent mechanism and controlling dynamic leading process branching and nucleokinesis via a PRD2-dependent mechanism. To provide additional evidence that the GAP and PRD2 domains of OPHN1 have independent roles, we tested whether the migration defect caused by OPHN1 depletion could be rescued by coexpressing both the OPHN1^{GAP*} and OPHN1^{PRD2*} mutants with

Downloaded from on November 2, 2026 - Published by Cold Spring Harbor Laboratory Press

Ophn1#2 shRNA. Consistent with independent functions of the GAP and PRD2 domains, coexpression of OPHN1^{GAP*} and OPHN1^{PRD2*} rescued the migration defect caused by OPHN1 depletion (Supplemental Fig. S5A,B).

OPHN1-GAP regulates MP-to-BP transition by suppressing the RHOA–ROCK pathway

Our data reveal that the GAP domain of OPHN1 is critical for the MP-to-BP transition of cortical projection neurons. To investigate how the OPHN1-GAP domain regulates this process, we tested whether it acts by antagonizing RHOA signaling. Although previous in vitro GTPase assays showed that OPHN1 can reduce the levels of active RHOA, RAC1, and CDC42 (Billuart et al. 1998; Govek et al. 2004), the OPHN1^{GAP*} mutant most closely phenocopied the effects of elevated RHOA signaling, characterized by impaired MP-to-BP transition and consequently defective radial migration (Nguyen et al. 2006; Govek et al. 2011; Pacary et al. 2011; Cappello et al. 2012; Koch et al. 2014; Tang et al. 2014; Xu et al. 2019). Therefore, we coelectroporated a dominant-negative (DN) *RHOA* (*RHOA^{N19}*)-expressing construct together with vectors expressing Ophn1#2 shRNA and *OPHN1^{GAP*}-EGFP* into E14 mouse cortices and analyzed the distribution and morphology of transfected cells 4 days later. We found that RHOA^{N19} rescued the MP-to-BP transition defect of neurons with impaired OPHN1 Rho-GAP activity (Fig. 6A–C), indicating that OPHN1-GAP regulates this step by suppressing RHOA activity, thereby restoring neuronal migration.

Key downstream effectors of RHOA involved in actin cytoskeleton regulation and implicated in the polarization of newborn neurons are the Rho-associated coiled-coil-containing protein kinase (ROCK) family of serine/threonine kinases, also known as Rho-kinases (Uehata et al. 1997; Amano et al. 2000; Pacary et al. 2011). The ROCK family comprises two members, ROCK1 and ROCK2, both of which are expressed in newborn cortical neurons (Riento and Ridley 2003; Govek et al. 2011; Xu et al. 2019). To test whether ROCK proteins mediate the effects of OPHN1-GAP on MP-to-BP polarization, we depleted both ROCK1 and ROCK2 and examined whether this rescued the defect caused by impaired OPHN1-GAP activity. We generated mir-30-based shRNA vectors targeting *Rock1* and *Rock2* and validated their efficacy in HEK293T cells (Fig. 6D). Vectors expressing Rock1#1 and Rock2#2 shRNAs were then coelectroporated into E14 mouse cortices together with vectors expressing *OPHN1^{GAP*}-EGFP* and Ophn1#2 shRNA, and neuronal distribution and morphology were analyzed 4 days later. Coexpression of Rock1#1 and Rock2#2 shRNAs rescued the MP-to-BP transition defect resulting from loss of OPHN1-GAP activity, thereby restoring neuronal migration (Fig. 6E–G). Taken together, these findings demonstrate that OPHN1-GAP regulates the MP-to-BP transition by suppressing the RHOA/ROCK pathway, a step required for proper subsequent radial neuronal migration.

OPHN1-PRD2 interacts with PACSIN2

In addition to its GAP-dependent role in the MP-to-BP transition, our data reveal a GAP-independent, PRD2-dependent function of OPHN1 in regulating dynamic leading process branching and nucleokinesis. As no proteins have previously been reported to selectively interact with the PRD2 domain of OPHN1, we sought to identify candidate interactors to gain insight into its mechanism. To this end, we performed BioID (Roux et al. 2012) using OPHN1^{WT} and the OPHN1^{PRD2*}, OPHN1^{GAP*}, OPHN1^{PRD1*}, and OPHN1^{PRD3*} mutants to assess domain-specific interactions. We generated tetracycline-inducible HEK293 cell lines stably expressing N-terminal BirA*-FLAG-tagged OPHN1^{WT} or each mutant fusion protein (Supplemental Fig. S6A), and confirmed their expression by western blot and immunofluorescence (Supplemental Fig. S6B,C). After 24 h of labeling, biotinylated proteins were affinity-purified and analyzed by mass spectrometry (Supplemental Table S1). Given that proline-rich domains (PRDs) preferentially bind Src homology 3 (SH3) domain-containing proteins, we filtered the OPHN1^{WT} proximal proteome for SH3 domain-containing proteins using InterPro (Blum et al. 2025; Paysan-Lafosse et al. 2025), identifying 26 such proteins. Subsequent SAINTexpress scoring (Teo et al. 2014) revealed that five of them represent high-confidence putative OPHN1 interactors (SAINT score ≥0.9): ARHGAP10, MYH10, NEBL, PACSIN2, and SH3GL1 (Fig. 7A). We next assessed which of these candidates retained association with OPHN1^{GAP*}, OPHN1^{PRD1*}, and OPHN1^{PRD3*}, but not with OPHN1^{PRD2*}, in the mutant BioID data sets. PACSIN2 was the only candidate that met this criterion (Fig. 7B). To further substantiate the selective binding of PACSIN2 SH3 domain to the PRD2 domain of OPHN1, we performed GST pull-down assays using lysates from HEK293T cells expressing GFP-tagged OPHN1^{WT} or the respective OPHN1 mutants. Recombinant GST-PACSIN2-SH3 efficiently pulled down OPHN1^{WT}, OPHN1^{PRD1*}, OPHN1^{PRD3*}, and OPHN1^{GAP*}, but not OPHN1^{PRD2*} (Fig. 7C), demonstrating that PACSIN2 is a PRD2-specific interactor of OPHN1.

PACSIN2 (protein kinase C and casein kinase substrate in neurons protein 2; also known as Syndapin II) is a member of the Pacsin family of F-BAR domain-containing adaptor proteins involved in membrane remodeling, actin cytoskeleton organization, and endocytosis (Dumont and Lehtonen 2022). These functions, however, have been characterized primarily in nonneuronal cells, and its role in the developing neocortex has not been examined. Therefore, before functionally characterizing PACSIN2's role in cortical projection neuron migration (see below), we first examined its expression in the embryonic neocortex. Immunohistochemistry on E16 coronal brain sections revealed that, like OPHN1, PACSIN2 is expressed in Nestin-positive progenitors and is prominent in newborn cortical projection neurons (Fig. 7D). Moreover, PACSIN2 exhibits a localization pattern similar to that of OPHN1, localizing to vesicular structures

Downloaded from on November 2, 2026 - Published by Cold Spring Harbor Laboratory Press

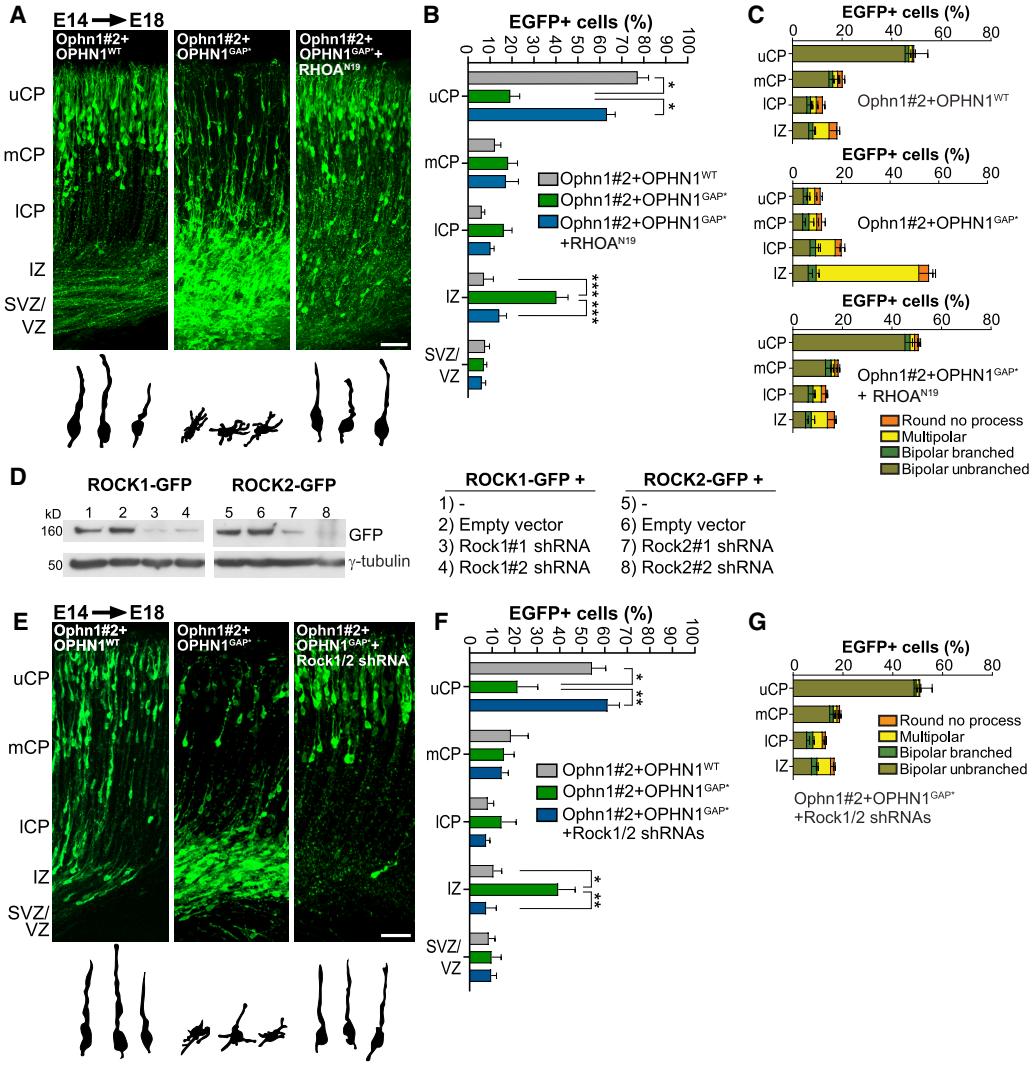


Figure 6. OPHN1-GAP promotes MP-to-BP transition via RHOA–ROCK pathway inhibition. (*A*) Representative confocal images of E18 neocortices electroporated at E14 with vectors expressing Ophn1#2 shRNA together with *OPHN1^{WT}-EGFP*, *OPHN1^{GAP*}-EGFP*, or *OPHN1^{GAP*}-EGFP* plus *RHOA^{N19}*, showing the distribution of EGFP$^+$ transfected cells across the indicated regions of the developing neocortex. Scale bar, 50 µm. Computer-based reconstructions of representative neurons in the IZ/lCP are shown at the *bottom*. (*B*) Quantification of the percentage of EGFP$^+$ cells in each region. Data are presented as mean ± SEM; $n = 3$–4 brains per condition. (*) $P < 0.05$, (***) $P < 0.001$, one-way ANOVA with Tukey–Kramer post hoc test. (*C*) Percentage of EGFP$^+$ cells exhibiting bipolar morphology with an unbranched or branched leading process, multipolar morphology, or round morphology lacking processes. Data are mean ± SEM. $n = 4$–5 brains per condition. (*D*) Validation of miR30-based shRNAs against *Rock1* and *Rock2*. Western blot of total lysates from HEK293T cells cotransfected with a plasmid expressing *Rock1-EGFP* or *Rock2-EGFP* and one of the indicated RNAi constructs, probed with antibodies to GFP and γ-tubulin as a loading control. (*E*) Representative confocal images of E18 neocortices electroporated at E14 with vectors expressing Ophn1#2 shRNA together with *OPHN1^{WT}-EGFP*, *OPHN1^{GAP*}-EGFP*, or *OPHN1^{GAP*}-EGFP* plus *Rock1/2*-targeting shRNAs (Rock1#1+Rock2#2), showing the distribution of EGFP$^+$ transfected cells across the indicated regions of the developing neocortex. Scale bar, 50 µm. Computer-based reconstructions of representative neurons in the IZ/lCP are shown at the *bottom*. (*F*) Quantification of the percentage of EGFP$^+$ cells in each region. Data are presented as mean ± SEM; $n = 3$–4 brains per condition. (*) $P < 0.05$, (**) $P < 0.01$, one-way ANOVA with Tukey–Kramer post hoc test. (*G*) Percentage of EGFP$^+$ cells exhibiting the indicated morphologies. Data are presented as mean ± SEM; $n = 5$ brains per condition.

surrounding the nucleus and to the tips of neuronal processes, where it colocalizes with OPHN1 in dissociated cortical projection neurons (Fig. 7E). Together, these data identify PACSIN2 as a novel interactor of OPHN1-PRD2 and a potential mediator of its role in cortical migration.

PACSIN2 mediates the OPHN1-PRD2-dependent regulation of leading process branching and nucleokinesis during cortical projection neuron locomotion

To assess the functional relevance of the OPHN1-PRD2–PACSIN2 interaction, we reasoned that if this interaction

Downloaded from on November 2, 2026 - Published by Cold Spring Harbor Laboratory Press

is required for cortical projection neuron migration, then depleting PACSIN2 should phenocopy the migration defects observed in neurons expressing OPHN1$^{PRD2^*}$ in an *Ophn1* RNAi background. To test this, we generated vectors coexpressing *EGFP* and miR30-based shRNAs targeting *Pacsin2* or a control sequence. The efficiency of the *Pacsin2*-targeting shRNAs was confirmed by western blot in HEK293T cells (Fig. 8A). Control (scr#2) or Pacsin2#2 or Pacsin2#3 shRNA-expressing vectors were then introduced into E14 embryonic cortices via IUE, and neuronal distribution was assessed at E18. Similar to OPHN1$^{PRD2^*}$-expressing neurons, most neurons expressing either *Pacsin2* shRNA underwent the MP-to-BP transition, but a substantial number remained stalled in the lower and middle CP (Fig. 8B,C). In addition, many of these neurons exhibited an aberrantly branched leading process (Fig. 8D,E) and impaired attachment to radial glial fibers (Supplemental Fig. S2A,B).

We next performed live-cell imaging to corroborate these findings. The majority of PACSIN2-depleted neurons, while able to undergo the MP-to-BP transition and traverse the IZ, exhibited minimal movement in the lower CP and showed extensive leading process branching throughout the 13 h imaging period (Fig. 8F–H;

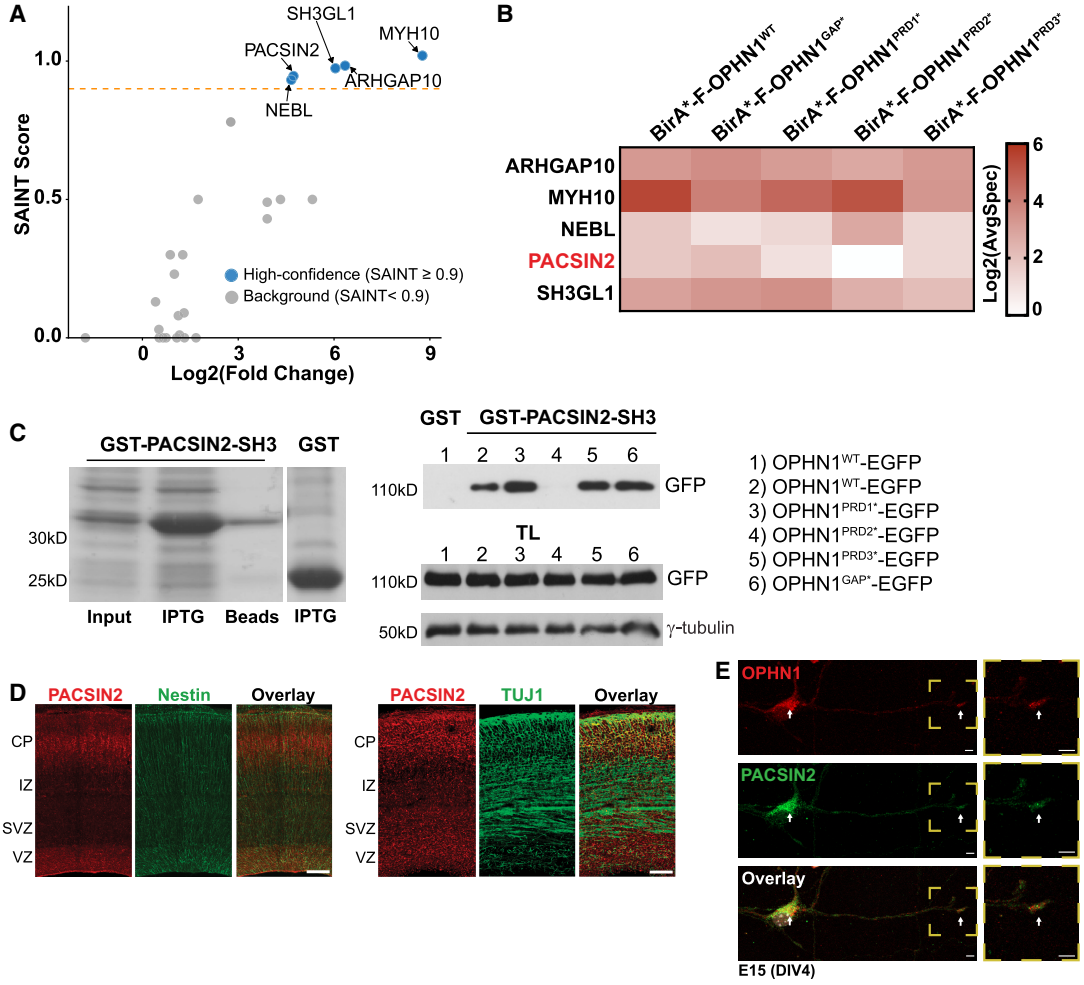


Figure 7. OPHN1-PRD2 interacts with PACSIN2. (*A*) Scatter plot comparing SAINT score and $\log_2$ fold change (over control) for the 26 SH3 domain-containing proteins detected in the BirA*-FLAG-OPHN1^{WT} BioID experiment. High-confidence interactors (SAINT score ≥0.9) are highlighted in blue. (*B*) Heat map showing relative protein abundance of the five high-confidence SH3 domain-containing candidate interactors of OPHN1^{WT}, represented as $\log_2$ transformed average spectral count (AvgSpec) across BirA*-FLAG-OPHN1^{WT} and the indicated OPHN1 domain mutants. PACSIN2 (highlighted in red) is the only prey protein that shows loss of enrichment in the BirA-F-OPHN1$^{PRD2^*}$ bait condition. (*C*) Validation of the OPHN1–PACSIN2 interaction by GST pulldown assay. (*Right* panel) GST-PACSIN2-SH3 fusion protein or GST alone (Coomassie blue staining), immobilized on beads, was incubated with lysates from HEK293T cells transfected with vectors encoding *OPHN1^{WT}-EGFP*, *OPHN1$^{PRD1^*}$-EGFP*, *OPHN1$^{PRD2^*}$-EGFP*, *OPHN1$^{PRD3^*}$-EGFP*, or *OPHN1$^{GAP^*}$-EGFP*. Bound OPHN1 (WT or mutant) was detected by immunoblotting using an anti-GFP antibody. γ-Tubulin served as a loading control. (TL) Total lysate. (*D*) Coronal sections of E16 mouse neocortex immunostained for PACSIN2 and the neural stem/progenitor marker Nestin or the early neuronal marker βIII-tubulin (TUJ1). Scale bars, 50 µm. (*E*) Cultured cortical neurons (DIV4) isolated from E15 neocortices and immunostained for OPHN1 and PACSIN2. *Right* panels show enlarged views of the boxed tips of the neuronal processes. Arrows indicate regions of strong overlapping OPHN1 and PACSIN2 immunoreactivity. Scale bars, 5 µm.

Downloaded from on November 2, 2026 - Published by Cold Spring Harbor Laboratory Press

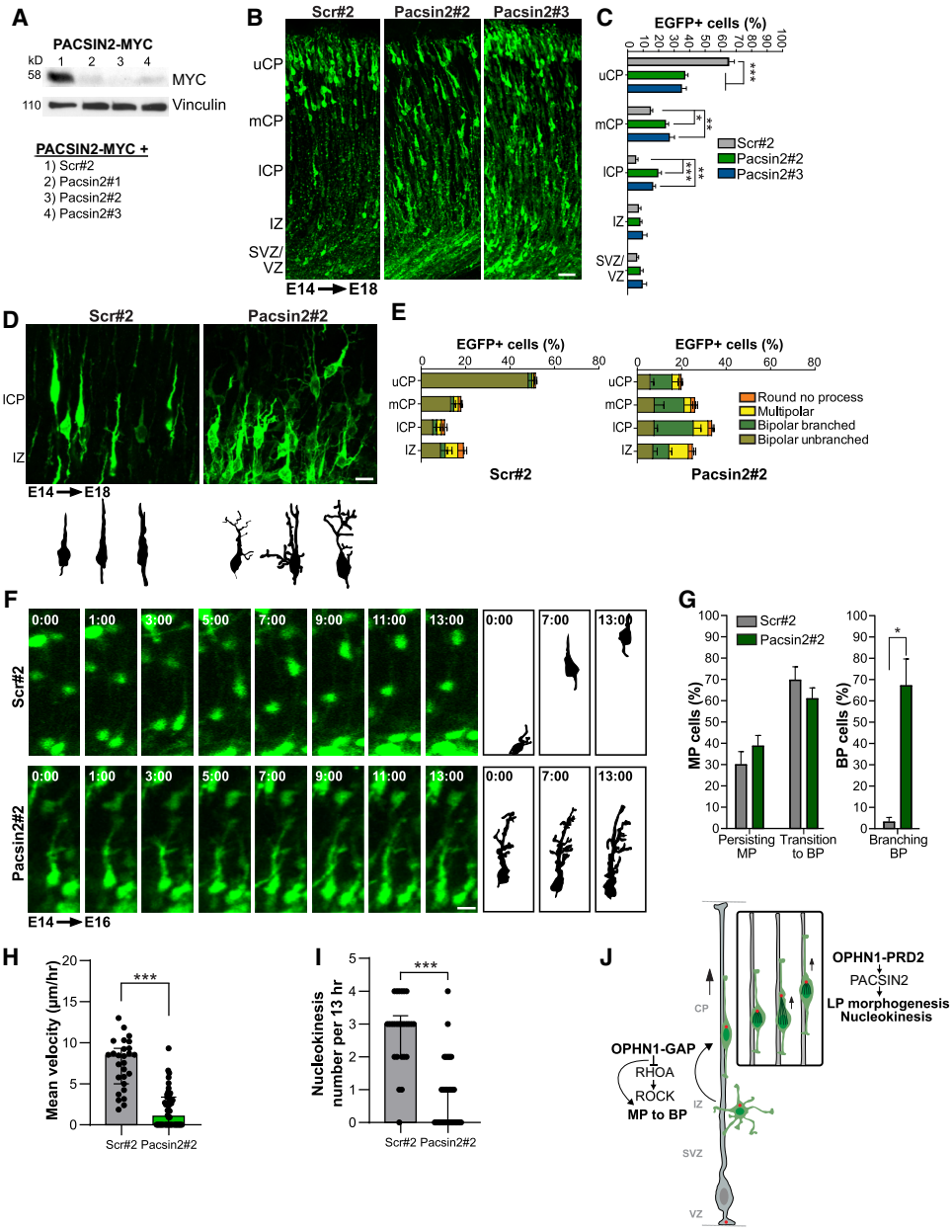


Figure 8. PACSIN2 depletion phenocopies the OPHN1-PRD2 mutant phenotype. (*A*) Validation of miR30-based shRNAs against *Pacsin2*. Western blot of total lysates from HEK293T cells cotransfected with a plasmid expressing *Pacsin2-MYC* and one of the indicated RNAi constructs, probed with antibodies to MYC and Vinculin as a loading control. (*B*) Representative confocal images of E18 neocortices electroporated at E14 with an *EGFP*-expressing vector together with a vector expressing scr#2, Pacsin2#2, or Pacsin2#3 shRNA, showing the distribution of EGFP$^+$ transfected cells across the indicated regions of the developing neocortex. Scale bar, 50 µm. (*C*) Quantification of the percentage of EGFP$^+$ cells in each region. Data are presented as mean ± SEM; $n = 4$–6 brains per condition. (*) $P < 0.05$, (**) $P < 0.01$, (***) $P < 0.001$, one-way ANOVA with Tukey–Kramer post hoc test. (*D*) Representative high-magnification images and computer-based reconstructions of neurons in the IZ and lCP of E18 neocortices electroporated at E14 with vectors expressing PACSIN2 and scr#2 or Pacsin2#2 shRNA. Scale bar, 20 µm. (*E*) Percentage of EGFP$^+$ cells exhibiting bipolar morphology with an unbranched or branched leading process, multipolar morphology, or round morphology lacking processes in the indicated regions of the developing neocortex. Data are presented as mean ± SEM; $n = 4$–5 brains per condition. (*F*) Time-lapse images acquired over 13 h period, performed 2 days after E14 coelectroporation with vectors expressing EGFP and either scr#2 or Pacsin2#2 shRNA, showing representative transfected neurons as they exit the IZ and enter the CP. Scale bar, 20 µm. (*Right*) Computer-based reconstructions of migrating neurons at the start of the recording and at 7 and 13 h. (*G*) Quantification of the percentage of *EGFP*$^+$ neurons that remained multipolar (MP) or transitioned to a bipolar (BP) morphology, and of BP neurons exhibiting a branched leading process during the 13 h recording period. Data are presented as mean ± SEM; $n = 26$–38 cells per condition pooled from four independent IUEs. (*) $P < 0.05$, Student's *t*-test with Welch's correction. (*H*,*I*) Quantifications of mean migration velocity (*H*) and number of nucleokinesis events per 13 h (*I*) in neurons expressing the indicated constructs. Data are presented as median (IQR); $n =$ 26–38 cells per condition pooled from four independent IUEs. (***) $P < 0.001$, Mann–Whitney *U*-test. (*J*) Summary schematic illustrating how OPHN1 governs radial migration through distinct domains and mechanisms. Its Rho-GAP domain controls the MP-to-BP transition by suppressing the RHOA/ROCK pathway, whereas its second PRD (PRD2) regulates leading process (LP) morphogenesis and nucleokinesis through interaction with PACSIN2.

Downloaded from on November 2, 2026 - Published by Cold Spring Harbor Laboratory Press

Supplemental Movie S6). Furthermore, as in neurons expressing OPHN1$^{PRD2^*}$, the number of nucleokinesis events was markedly reduced compared to the control scr#2 shRNA group (Fig. 8I). Analysis of centrosome and soma dynamics revealed that both remained largely stationary over the imaging period in PACSIN2-depleted neurons, phenocopying the behavior of OPHN1$^{PRD2^*}$-expressing neurons (Supplemental Fig. S7A–C).

Combined with our biochemical data showing that PACSIN2 specifically interacts with the PRD2 domain of OPHN1, these findings support a key role for PACSIN2 in mediating the PRD2-dependent function of OPHN1 during the locomotion phase of projection neuron migration, particularly in the regulation of leading process branching and nucleokinesis.

Discussion

Critical to the establishment of proper functional connectivity in the developing neocortex is the tightly regulated, multistep migration of excitatory projection neurons, including the MP-to-BP transition and subsequent glial-guided locomotion. Although progress has been made in identifying regulators of individual stages of radial migration, how these sequential steps are coordinated at the molecular level remains poorly understood. Here, we identify OPHN1, a multidomain Rho-GAP and member of the GRAF family, as a dual-function regulator of radial migration that governs both the MP-to-BP transition and subsequent locomotion. OPHN1 controls these successive steps through distinct domains and interaction partners: its GAP domain promotes the MP-to-BP transition by antagonizing RHOA–ROCK signaling, whereas its second proline-rich domain (PRD2) regulates leading process branching and nucleokinesis during locomotion via interaction with PACSIN2 (Fig. 8J).

Initially identified through the analysis of a balanced t(X;12) translocation in a female patient with mild intellectual disability (ID) (Billuart et al. 1998), mutations in *OPHN1* have since been linked to a syndromic form of ID typically accompanied by developmental delay, behavioral abnormalities, seizures, and structural brain abnormalities (Billuart et al. 1998; Tentler et al. 1999; Bergmann et al. 2003; Philip et al. 2003; des Portes et al. 2004; Chabrol et al. 2005; Zanni et al. 2005; Pirozzi et al. 2011; Santos-Rebouças et al. 2014; Moortgat et al. 2018; Schwartz et al. 2019). Although OPHN1 has been extensively studied in dendritic spine development, synaptic plasticity, and more recently postnatal/adult neurogenesis (Govek et al. 2004; Khelfaoui et al. 2007, 2009, 2014; Nadif Kasri et al. 2009, 2011; Nakano-Kobayashi et al. 2009, 2014; Powell et al. 2012; Compagnucci et al. 2016; Redolfi et al. 2016; Allegra et al. 2017; Zhang et al. 2017; Wang et al. 2021; Cresto et al. 2022; Kawa et al. 2022), its role in early cortical development has remained largely unexplored. We found that OPHN1 is prominently expressed in the developing neocortex during periods of active neurogenesis and neuronal migration. To investigate its developmental function, we employed an acute depletion strategy designed to minimize the compensatory effects often associated with germline knockout models (Deuel et al. 2006; Corbetta et al. 2009; Valiente and Marín 2010), particularly given that OPHN1 belongs to a family of four closely related GRAF proteins. Using this approach, we uncovered a cell-autonomous role for OPHN1 in regulating cortical projection neuron migration. Of note, our finding that acute OPHN1 depletion results in persistent migration defects raises the possibility that impaired neuronal migration may contribute to some of the brain abnormalities associated with *OPHN1*-related disorder (Biswas et al. 2026).

Our domain-specific molecular replacement studies further revealed a dual role for OPHN1 in regulating successive stages of cortical projection neuron migration through distinct molecular mechanisms. Notably, these distinct functions would have remained obscured by depletion studies alone, as early stalling in the IZ masks later requirements during locomotion. We found that the GAP domain of OPHN1, previously shown to suppress RHOA activity in neurons, is essential for the MP-to-BP transition. This is consistent with prior studies demonstrating that precise control of RHOA activity is required for neuronal polarization, with elevated RHOA activity hampering this step (Govek et al. 2005; Nguyen et al. 2006; Pacary et al. 2011; Koch et al. 2014; Tang et al. 2014; Xu et al. 2019). Our findings position OPHN1 as a key upstream regulator of RHOA and its downstream effector ROCK (Amano et al. 1996) during this developmental transition. Indeed, suppression of RHOA–ROCK signaling rescued the MP-to-BP transition impaired by loss of OPHN1-GAP activity, thereby restoring subsequent neuronal migration. As to how suppression of this pathway facilitates the MP-to-BP transition, a major downstream effector of RHOA–ROCK signaling in actin cytoskeleton remodeling is nonmuscle myosin II (Amano et al. 1996; Kimura et al. 1996). Previous work has shown that activation of nonmuscle myosin II restrains neuronal polarization by promoting the formation of actin arcs and preventing microtubule protrusion into the nascent axon growth cone (Dupraz et al. 2019). Building on these findings, a plausible scenario is that OPHN1 facilitates the MP-to-BP transition by suppressing RHOA–ROCK activity, thereby limiting myosin II-dependent actin arc formation and enabling neuronal polarization.

In contrast to the early migration block observed with the OPHN1$^{GAP^*}$ mutant, we found that disruption of the PRD2 domain does not impair early polarization but compromises locomotion within the cortical plate. Neurons expressing the OPHN1$^{PRD2^*}$ mutant exhibit excessive leading process branching, impaired attachment to radial glial fibers, and defective nucleokinesis, highlighting a distinct requirement for PRD2 during glial-guided migration. Until now, the function of the OPHN1-PRD2 domain and identity of its interacting partners remained unknown. Our data identify PACSIN2 as a selective PRD2-binding partner and provide multiple lines of evidence supporting the functional relevance of this interaction in cortical migration. Both proteins are coexpressed

Downloaded from on November 2, 2026 - Published by Cold Spring Harbor Laboratory Press

in migrating cortical projection neurons and colocalize within vesicular compartments surrounding the nucleus and at the tips of neuronal processes. Most importantly, PACSIN2 depletion phenocopies the locomotion defects observed upon OPHN1-PRD2 disruption, including excessive leading process branching, reduced attachment to radial glial fibers, and impaired nucleokinesis.

How the interaction between PACSIN2 and OPHN1 controls the locomotion of cortical projection neurons remains to be fully elucidated. However, given the established roles of PACSIN2 in regulating both actin cytoskeleton dynamics and vesicular/endosomal trafficking (Qualmann and Kelly 2000; Braun et al. 2005; Kessels and Qualmann 2006; Grimm-Gunter et al. 2008; Wang et al. 2009; de Kreuk et al. 2011; Quan and Robinson 2013; Dorland et al. 2016; Dumont and Lehtonen 2022), PACSIN2 is well positioned to coordinate the membrane and cytoskeletal remodeling events that govern radial glia-guided locomotion (Marin and Rubenstein 2003; Solecki et al. 2006; Govek et al. 2011; Cooper 2013; Lian and Sheen 2015). Mechanistically, as an adaptor protein capable of oligomerization via its F-BAR domain (Snider et al. 2021), PACSIN2 may assemble localized signaling complexes that spatially coordinate adhesion dynamics and cytoskeletal rearrangements during locomotion. An additional layer of regulation is highlighted by the finding that PACSIN2 is regulated by intramolecular SH3–F-BAR autoinhibition (Senju et al. 2011). A possible model is that binding of OPHN1 to the PACSIN2 SH3 domain relieves this autoinhibition, thereby enabling spatially and temporally restricted PACSIN2 function during locomotion. Future studies will be needed to test this model and further define how OPHN1 and PACSIN2 cooperate to facilitate glial-guided locomotion.

In summary, our findings uncover a previously unrecognized role for OPHN1 in early cortical development, demonstrating that it orchestrates successive phases of cortical projection neuron migration through domain-specific mechanisms. While the GAP domain regulates the MP-to-BP transition via RHOA–ROCK signaling, the PRD2 domain governs locomotion through its newly identified interaction with PACSIN2. This modular organization illustrates how distinct domains within a single protein can coordinate sequential steps in neuronal migration, a process essential for the assembly of functional cortical circuits.

Materials and methods

cDNA and RNAi constructs

pCA-*OPHN1*^{WT}-*EGFP*, pCA-*OPHN1*^{GAP*}-*EGFP*, pCA-*OPHN1*^{PRD1*}-*EGFP*, pCA-*OPHN1*^{PRD2*}-*EGFP*, and pCA-*OPHN1*^{PRD3*}-*EGFP* were generated by cloning full-length wild-type *OPHN1* or full-length *OPHN1* cDNAs carrying mutations in the indicated domains into the pCAG-*EGFP* vector (gift from Wilson Wong; Addgene plasmid # 89684; http://n2t.net/addgene:89684; RRID:Addgene_89684). pND1-*EGFP*, pND1-*OPHN1*^{WT}-*EGFP*, and pND1-dsRed were constructed by cloning *EGFP, OPHN1*^{WT}, or dsRed cDNAs into pNeuroD1 (gift from Franck Polleux). BirA-FLAG-*OPHN1*^{WT}, BirA-FLAG-*OPHN1*^{GAP*}, BirA-FLAG-*OPHN1*^{PRD1*}, BirA-FLAG-*OPHN1*^{PRD2*}, and BirA-FLAG-*OPHN1*^{PRD3*} were generated by cloning into the pcDNA5-pDEST-FRT vector. pEGFP-C1-*Rock1-GFP*, pEGFP-C1-*Rock2-GFP* were gifts from Alpha Yap (Addgene plasmid 187296, http://n2t.net/addgene:187296; and RRID:Addgene_187296 and 101296, http://n2t.net/addgene:101296; RRID:Addgene_101296, respectively). pcDNA3-*MYC-RHOA*^{T19N} was a kind gift from Dr. Richard Cerione. pCMV-*MYC-Pacsin2* and pGST-PACSIN2-SH3 were kind gifts from Dr. Markus Plomann and have been described previously (Modregger et al. 2000). For RNAi knockdown experiments, DNA fragments encoding short hairpin RNAs (shRNAs) directed against mouse *Ophn1* mRNA were described previously (Nadif Kasri et al. 2009). Briefly, *Ophn1*#1 (5′-GAACCTATCTACCA CACTC-3′), *Ophn1*#2 (5′-GAAGAGCAGCTCTTTCT GG-3′), and control shRNA scr#1 (5′-GCTCACCCTTCC TACTCTC-3′) were cloned into the pSUPER.basic vector (oligoengine). For RNAi knockdown of *Rock1, Rock2*, and *Pacsin2*, the following target sequences were inserted into the pCA-EGFP-miR30 vector: Rock1#1 (5′-TTTAT TTCCTGTTTCATCTGTT-3′), Rock1#2 (5′-TTTAATTG CATTTCATTATGCA-3′), Rock2#1 (5′-TGATTTAGCT TCTTCAATGGAT-3′), Rock2#2 (5′ TTACTCATAAGG TTGACGAGGT-3′), Pacsin2#2 (5′-TTGCATTTTTC TATCTTGTCTT-3′), and Pacsin2#3 (5′-TCAAAGTCTTC ATTCATCAGTG-3′). For time-lapse imaging experiments, pCA-DsRed-Express-*Centrin-1* (kind gift from Dr. Songhai Shi), pCAG-LPL-Lyn-EGFP, and pCAG-Cre were used in combination with the indicated RNAi and rescue plasmids.

Cell culture and transfection

HEK293T cells and stable Flp-In T-REx HEK293 cells (Thermo Fisher Scientific) were maintained in DMEM supplemented with 10% fetal bovine serum (FBS) and 1% penicillin–streptomycin in a humidified incubator at 37°C with 5% CO_2. HEK293T cells were transfected using Lipofectamine 2000 (Thermo Fisher Scientific). Stable Flp-In T-REx HEK293 cell lines expressing N-terminal BirA*-FLAG-tagged OPHN1^{WT} or OPHN1 mutant fusion proteins were generated using the Flp-In T-REx system according to the manufacturer's instructions (Thermo Fisher Scientific). BirA-FLAG was fused to the N terminus of OPHN1 to preserve accessibility of its C-terminal proline-rich domains. Briefly, pcDNA5-pDEST-FRT-BirA*-FLAG-*OPHN1* plasmids were cotransfected with the Flp recombinase expression vector pOG44 into Flp-In T-REx HEK293 cells at ~80% confluence using Lipofectamine 2000, and stable integrants were selected with hygromycin for 2–3 weeks. Protein expression was induced with 1 µg/mL tetracycline for 24 h. For BioID experiments, cells were incubated with tetracycline and 50 µM biotin for 24 h before harvest.

Cultured cortical neurons were prepared from embryonic day (E) 15.5 C57BL/6 mouse cortices. Briefly, cortices

Downloaded from on November 2, 2026 - Published by Cold Spring Harbor Laboratory Press

were dissected into dishes containing dissociation medium consisting of 97.5% Hank's balanced salt solution (HBSS; Gibco), 1 mM sodium pyruvate (Sigma-Aldrich), 0.1% glucose, and 10 mM HEPES (pH 7.3; Gibco). They were then digested in fresh dissociation medium containing a final concentration of 0.05% trypsin/EDTA for 20 min at 37°C, followed by the addition of 0.5 mL of DNase I solution and incubation for 5 min at room temperature. Tissue was subsequently washed with fresh dissociation medium and resuspended in plating media consisting of 86.55% DMEM, 10% heat-inactivated fetal bovine serum, 0.45% glucose, 1 mM sodium pyruvate, 1% GlutaMAX (Gibco), and 1% penicillin–streptomycin. Tissue was gently triturated using a fire-polished glass Pasteur pipette, and the resulting cell suspension was passed through a 70 µm sterile nylon cell strainer. Cells were plated at a density of 2.5×10^4 to 5×10^4 cells per well on 12 mm coverslips (Assistent) precoated with 0.02 mg/mL poly-D-lysine. After 2 h, plating medium was replaced with maintenance medium consisting of 96% neurobasal (Gibco), 2% B-27 (Gibco), 1% penicillin–streptomycin, and 1% GlutaMAX. Neurons were maintained at 37°C in a humidified incubator with 5% CO_2, and half of the medium was replaced every 4 days.

In utero electroporation (IUE) and BrdU administration

IUE was performed largely as previously described (Yang et al. 2012). Briefly, timed pregnant CD1 mice (Charles River) at E14 were anesthetized and the uterine horns were exposed. Approximately 1–2 µL of plasmid DNA was injected into the lateral ventricles of the embryos using a beveled, calibrated glass micropipette. Five 50 msec pulses of 40 V were delivered at 950 msec intervals using 3.5 mm electrode paddles positioned on either side of the embryonic head (BTX ECM830). After electroporation, the uterine horns were returned to the abdominal cavity, and the incision was surgically sutured. For BrdU labeling experiments, embryos were electroporated at E14, and BrdU (150 mg/kg body weight) was administered at E17. Animals were sacrificed 2 h later. All procedures were approved by the Cold Spring Harbor Laboratory Animal Care and Use Committee.

Immunofluorescence and immunohistochemistry

For immunostaining of 4 day in vitro (DIV4) cortical neurons, neurons isolated from E15 mouse cortices were plated on coverslips coated with poly-D-lysine. Neurons were fixed in 4% paraformaldehyde (PFA), followed by permeabilization in 0.1% Triton X-100 and blocking in PBS containing 5% normal goat serum (NGS). Cells were incubated overnight at 4°C with primary antibodies diluted in PBS containing 5% NGS and 0.1% Triton X-100. The following primary antibodies were used: anti-OPHN1 (mouse mAb IgG2a, 1:100; Santa Cruz Biotechnology [F-3] sc-376037), anti-NeuN (mouse mAb IgG1, 1:500; Millipore MAB377), and anti-PACSIN2 (rabbit mAb, 1:250; Proteintech 84763-4-RR). After washing, cells were incubated with the appropriate Alexa Fluor-conjugated goat secondary antibodies for 2 h at room temperature, and coverslips were mounted with Fluoromount-G mounting medium (Thermo Fisher Scientific). Images were acquired using a Zeiss LSM800 confocal microscope equipped with a 63× oil objective (1.4 NA).

For immunostaining of stable Flp-In T-REx HEK293 cells, cells were plated on coverslips overnight in the presence of 1 µg/mL tetracycline and 50 µM biotin prior to fixation. Cells were washed with PBS and fixed for 15 min with 3.7% formaldehyde prepared in CSK buffer (100 mM NaCl, 300 mM sucrose, 3 mM $MgCl_2$, 10 mM PIPES pH 6.8), followed by permeabilization with 0.1% Triton X-100 in PBS. Cells were then incubated with anti-FLAG (M2) antibody (mouse mAb IgG1, 1:150; Sigma-Aldrich F3165) diluted in TBS containing 1% BSA and 0.1% Triton-X100. After five washes with TBS, cells were incubated with Alexa Fluor 568 goat antimouse IgG secondary antibody together with Alexa Fluor 633 Streptavidin. Cells were subsequently washed 10 times with TBS, followed by a final wash in water before mounting the coverslips with Mowiol. Images were acquired with a DM6 upright microscope (Leica Microsystems) equipped with an ORCAflash 4.0V.2 monochromatic camera (Hamamatsu Photonics).

For immunostaining of brain sections, animals were deeply anesthetized with isoflurane and transcardially perfused with PBS followed by 4% PFA in 0.1 M phosphate buffer. Brains from embryos or P10 pups were fixed overnight at 4°C in 4% PFA in 0.1 M phosphate buffer and subsequently cryoprotected in 30% sucrose in PBS. Coronal brain sections (50 µm) were subsequently prepared using a Leica VT1000S Vibratome. Sections were blocked and permeabilized in PBS containing 10% normal goat serum (NGS) and 0.3% Triton X-100 for 30 min at room temperature, followed by overnight incubation at 4°C with primary antibodies diluted in PBS containing 10% NGS and 0.3% Triton X-100. The following primary antibodies were used: anti-OPHN1 (rabbit pAb, 1724, 1:100) (Govek et al. 2004), anti-Nestin (mouse mAb IgG1, 1:200; Chemicon MAB5326, and chicken pAb, 1:500; Aves Labs NES), anti-Tuj1 (mouse mAb IgG2a, 1:500; Covance MMS-435P), anti-GFP (chicken pAb, 1:500; Aves Labs GFP-1020), anti-BrdU (rat mAb IgG2a, 1:500; AbD Serotec OBT0030), anti-CUX1 (rabbit pAb, 1:500; Santa Cruz Biotechnology SC-13024); anti-CTIP2 (rat mAb IgG2a, 1:500; Abcam ab18465), and anti-RFP (rabbit pAb, 1:500; Rockland 600-401-379). Sections were incubated with the appropriate Alexa Fluor-conjugated secondary antibodies for 2 h at room temperature and mounted with Fluoromount-G mounting medium. Nuclei were counterstained with 0.3 µg/mL 4′,6-diamidino-2-phenylindole (DAPI; Sigma) during secondary antibody incubation. All sections were counterstained with DAPI, although DAPI images were not always included in the figures for clarity. Images were acquired using a Zeiss LSM 800 confocal microscope equipped with 20× dry (0.4 NA) and 63× oil (1.4 NA) objectives.

Downloaded from on November 2, 2026 - Published by Cold Spring Harbor Laboratory Press

Quantitative analyses of electroporated fixed brain slice preparations

All image quantifications were performed by investigators blinded to experimental conditions.

BrdU, TUJ1, CUX1*, and CTIP2 quantifications* Anatomically matched coronal sections from electroporated brains were immunostained with the indicated antibodies and imaged under identical acquisition settings. Distinct cortical regions were identified based on DAPI staining, cell density, and marker distribution. For each section, the electroporated area was defined by EGFP expression, and marker-positive cells were quantified within the EGFP$^+$ population. BrdU and TUJ1 quantifications were expressed as the percentage of EGFP$^+$ cells positive for the indicated marker. For laminar fate analyses, the percentages of EGFP$^+$ cells positive for CUX1 and CTIP2 were determined within the cortical plate or the indicated cortical regions. At least three adjacent anatomically matched sections were analyzed per brain, and the mean value for each brain was used for statistical analyses.

Nestin$^+$ radial glial fibers Coronal sections immunostained with anti-Nestin antibodies were analyzed in electroporated cortices. Only sections containing EGFP$^+$ neurons were included. A 200 µm-wide radial column was positioned perpendicular to the ventricular surface in anatomically matched regions across brains, and the number of Nestin-positive radial glial fibers intersecting a line spanning the width of the column was quantified at three defined distances from the ventricular zone using FIJI/ImageJ. Values were expressed as the number of Nestin$^+$ radial glial fibers per 200 µm, and the mean value obtained from all analyzed sections was used as a single biological replicate for each brain.

Percentage of leading processes as a function of distance from Nestin$^+$ radial glial fibers To assess the relationship between neuronal morphology and proximity to radial glial fibers, high-magnification (63×) images of EGFP$^+$ neurons in Nestin-immunostained sections were analyzed in anatomically matched cortical regions. For each neuron, the shortest distance between its leading process (branched or unbranched) and the nearest Nestin$^+$ radial glial fiber was measured. Three-dimensional reconstructions generated using Neurolucida 360 software (MBF bioscience) were used to quantify these distances. Distances were grouped into the indicated distance intervals, and the percentage of leading processes within each interval was determined. Mean values from all analyzed sections were calculated and used as a single value for each brain for statistical analysis.

Distribution of transfected cells across neocortical layers For distribution analyses, a 200 µm-wide radial column was positioned perpendicular to the ventricular surface in anatomically matched regions of the electroporated neocortex, and all EGFP$^+$ cells within this region were quantified. In embryonic brains, laminar boundaries were defined independently for each brain based on DAPI staining, differences in cell density, and cortical position. The cortex was subdivided into the ventricular zone (VZ), subventricular zone (SVZ), intermediate zone (IZ), and three equal subdivisions of the cortical plate: lower, middle, and upper cortical plate (lCP, mCP, and uCP). In representative figure panels, zone labels were positioned according to the laminar boundaries in the first image and applied at the same positions to subsequent images displayed at the same scale. Because the thickness of individual zones varied somewhat between brains, these labels served only as a reference for subsequent images and did not necessarily correspond precisely to the laminar boundaries of each individual image. For postnatal analyses, the distribution of EGFP$^+$ cells was quantified in the white matter (WM) and the lower, middle, and upper cortex (lC, mC, and uC). The number of EGFP$^+$ cells in each region was expressed as a percentage of the total number of EGFP$^+$ cells counted in the corresponding section. The mean percentage from all analyzed sections was calculated for each brain and used for statistical analysis.

Multipolar, bipolar branched, bipolar unbranched, and round process-lacking morphologies in IZ, lCP, mCP, and uCP For morphological analyses, high-magnification images of EGFP$^+$ neurons were acquired from the IZ and CP of electroporated neocortices. The CP was subdivided into lCP, mCP, and uCP. EGFP$^+$ neurons were classified into four morphological categories based on cell shape and process organization: round cells lacking obvious processes, multipolar (MP) cells bearing three or more processes extending from the cell body, bipolar unbranched (BP unbranched) cells with a bipolar morphology and a single unbranched leading process, and bipolar branched (BP branched) cells with a bipolar morphology and a branched leading process. For each region, the number of cells in each category was expressed as a percentage of the total number of EGFP$^+$ cells analyzed in that region. Reconstructions of representative neurons were generated with Adobe Illustrator from high-magnification confocal images.

Slice culture and time-lapse imaging

Time-lapse imaging of brain slices was performed largely as previously described (Bultje et al. 2009; Insolera et al. 2014) with minor modifications. Briefly, mouse embryos were electroporated at E14 with plasmids expressing the indicated constructs. Two days later, uterine horns containing the embryos were transferred to ice-cold complete HBSS consisting of 1× HBSS supplemented with 2.5 mM HEPES (pH 7.4), D-glucose, 1 mM $CaCl_2$, and 1 mM $MgSO_4$. Brains were dissected in ice-cold complete HBSS and embedded in 3% low-melting-point agarose prepared in complete HBSS, and coronal sections (250 µm) were prepared using a Leica VT1000S vibratome. Slices were transferred onto optically clear membrane inserts (Millicell, 30 mm, 0.4 µm pore size) precoated with 0.1 mg/

Downloaded from on November 2, 2026 - Published by Cold Spring Harbor Laboratory Press

mL poly-D-lysine (Sigma P6407-5MG) and maintained as organotypic cultures at 37°C in 5% CO_2. Slice culture medium consisted of basal medium Eagle supplemented with complete HBSS, D-glucose, 1 mM L-glutamine, 100 U/mL penicillin–streptomycin, and 5% horse serum. Slices were allowed to recover for ~2 h at 37°C in 5% CO_2 before being transferred to glass-bottom microwell dishes (MatTek). Samples were imaged using a Zeiss LSM780 confocal microscope equipped with an environmental chamber maintained at 37°C and 5% CO_2. Images were acquired every 15 min for ~13 h using a 20× long-working-distance dry objective (0.45 NA). Time-lapse movies were generated and analyzed using FIJI/ImageJ.

Quantitative analyses of time-lapse imaging

Time-lapse imaging data sets were analyzed to quantify neuronal migration dynamics and cellular morphology using a combination of manual annotation and semi-automated tracking in FIJI/ImageJ and Neurolucida 360. All analyses were performed on data sets acquired under similar imaging conditions, and only cells that remained within the field of view throughout the 13 h imaging period were included. Electroporated ($EGFP^+$) neurons located in the IZ and entering the CP were individually tracked and classified based on dynamic and morphological criteria into four categories: round, MP, BP unbranched, and BP branched. Persisting MP cells were defined by the presence of three or more dynamic processes and the absence of sustained radial migration throughout the imaging period. Cells were classified as transitioning to BP when they underwent a clear transition from MP to BP morphology, accompanied by stabilization of the leading and trailing processes and the onset of sustained directional migration. BP branched cells were defined as bipolar neurons that persistently extended secondary branches from the leading process within the CP. Classification was performed across the entire time series, and the percentage of cells in each category was calculated relative to the total number of tracked $EGFP^+$ neurons for each condition.

Mean velocity, nucleokinesis, and nucleus–centrosome analyses

Mean migration velocity was determined by tracking the position of the cell soma over the 13 h recording period. For each neuron, the total distance traveled by the soma was divided by the total duration of the recording to calculate mean migration velocity. Only neurons that could be unambiguously tracked throughout the imaging period were included. Values from individual cells were pooled across independent in utero electroporations and used for statistical comparisons between conditions. Nucleokinesis was quantified in time-lapse recordings by scoring discrete forward translocation events of the nucleus during the imaging period. Each event was defined as a discrete saltatory forward translocation of the nucleus followed by a pause phase. The total number of nucleokinesis events was determined for each tracked neuron over the full recording period, and the mean number of events was calculated for each experimental condition. Nucleus–centrosome coupling was analyzed in live-imaged neurons in which both the nucleus and centrosome could be clearly identified. Measurements were performed in cells coexpressing EGFP and the centrosomal marker DsRed-Express-Centrin1. At each time point, the distance between the center of the centrosome and the leading edge of the nucleus was measured in individual neurons. In addition, the cumulative distance traveled by the centrosome and the soma was quantified for each neuron. For each condition, nucleus–centrosome distances were averaged across all analyzed time points. Mean values were then calculated for each experimental condition.

BioID affinity purification and mass spectrometry (MS)

BioID experiments were performed as previously described (Bagci et al. 2020; Nahlé et al. 2022). Briefly, tetracycline- and biotin-treated HEK293 cells stably expressing N-terminal BirA*-FLAG-tagged OPHN1 fusion proteins were lysed in ice-cold RIPA lysis buffer supplemented with DTT, PMSF, and protease inhibitors. Cleared lysates were incubated with 70 µL of streptavidin beads (GE Healthcare 17-5113-01) for 3 h at 4°C. Beads were washed with lysis buffer followed by 50 mM ammonium bicarbonate (Biobasic AB0032, 500G). For on-bead digestion, 1 µg of trypsin (Sigma-Aldrich) was added to each 100 µL of sample in 50 mM ammonium bicarbonate and incubated overnight, followed by addition of another 1 µg of trypsin for 2 h. Supernatants were transferred to fresh microcentrifuge tubes, and the beads were washed twice with 100 µL of H_2O. The washes were pooled with the initial supernatant, acidified with formic acid (final concentration 5%; Sigma-Aldrich), and dried in a SpeedVac. Pellets were resuspended in 15 µL of 5% formic acid and stored at −80°C until analysis. Tryptic peptides were loaded onto a self-packed C18 column (75 µm internal diameter × 150 mm) installed on an Easy-nLC 1000 system (Proxeon Biosystems). Chromatography buffers consisted of 0.2% formic acid (buffer A) and 90% acetonitrile/0.2% formic acid (buffer B). Peptides were eluted at a flow rate of 250 nL/min using a two-step gradient in which buffer B increased from 2% to 35% over 100 min and then from 35% to 80% over 10 min. The liquid chromatography system was coupled to a Nanospray Flex ion source and an LTQ-Orbitrap Velos mass spectrometer (Thermo Fisher Scientific). Full-scan MS survey spectra (m/z 360–2000) were acquired in profile mode in the Orbitrap at a resolution of 60,000. The 15 most intense peptide ions were selected for fragmentation by collision-induced dissociation, and MS/MS spectra were acquired in the linear ion trap. Data were acquired across different experimental runs to minimize batch effects.

MS data analyses

Raw MS files from OPHN1 BioID samples were analyzed as previously described (Bagci et al. 2020) using the Mascot search engine through the iProphet pipeline integrated

Downloaded from on November 2, 2026 - Published by Cold Spring Harbor Laboratory Press

in ProHits and the RefSeq database supplemented with "common contaminants" from the Max Planck Institute, the Global Proteome Machine, and decoy sequences. Mascot search parameters included trypsin specificity with up to two missed cleavages allowed and oxidation (M) and deamidation (NQ) as variable modifications. Mass tolerances for precursor and fragment ions were set to 15 ppm and 0.6 kDa, respectively, and peptide charges of +2, +3, and +4 were considered. Mascot search results were individually processed using PeptideProphet, and peptides were assembled into proteins using parsimony rules originally described in ProteinProphet using the Trans-Proteomic Pipeline with the following parameters: -p 0.05 -x20 -PPM - "DECOY," iProphet option: pPRIME, and PeptideProphet: pP. Relative protein abundance across wild-type OPHN1 and domain-specific mutant data sets was determined by spectral counting. Sample reproducibility was assessed using Perseus from raw spectral counts of each biological replicate by calculating Pearson's correlation coefficients. Two replicates of each bait and each control (BirA* alone and BirA*-FLAG-EGFP) were used for each experiment.

Interaction scoring and bioinformatics analyses

Each OPHN1 proteomics data set (WT, GAP*, PRD1*, PRD2*, and PRD3*) was analyzed independently against its corresponding BirA* alone and BirA*-FLAG-EGFP control data sets within the ProHits suite, and SAINT-derived average probability (AvgP) scores were calculated. Across the individual OPHN1 data sets, 1129–1225 proteins were identified. To identify interactions potentially mediated by the proline-rich domains of OPHN1, proteins containing Src homology 3 (SH3) or SH3-like domains were first identified among proteins identified in the $OPHN1^{WT}$ proximal proteome based on their domain annotations in InterPro (Blum et al. 2025; Paysan-Lafosse et al. 2025). This filtering step yielded 26 SH3 domain-containing candidates. Subsequently, SAINTexpress was applied, identifying five high-confidence OPHN1 interactors (SAINT score ≥0.9). These high-confidence SH3 domain-containing candidates were then compared across the OPHN1 mutant data sets using mean spectral counts to assess domain-specific interactions.

GST pull-down assay

For pull-down experiments, expression of GST or GST fusion proteins was induced with IPTG in BL21 *Escherichia coli*. Bacteria were lysed and sonicated in lysis buffer containing 140 mM NaCl, 2.7 mM KCl, 10 mM Na_2HPO_4, 1.8 mM KH_2PO_4, and cOmplete protease inhibitor cocktail (Roche). GST-PACSIN2-SH3 fusion protein or GST alone was immobilized on glutathione-sepharose beads (GE Healthcare Biosciences). HEK293T cells expressing $OPHN1^{WT}$-GFP or OPHN1 mutant constructs were lysed in the same buffer, and equal amounts of lysate were incubated with GST-PACSIN2-SH3 or GST control beads. Bound proteins were analyzed by immunoblotting using anti-GFP (mouse mAb IgG2a, 1:500; NeuroMab N86/8). Anti-γ-tubulin (mouse mAb IgG1, 1:5000; Sigma GTU-88) was used as a loading control.

Western blot analyses

For western blot analyses of the developing cortex, mouse cortices (E11–P7) were homogenized with micropestles (Eppendorf) in lysis buffer containing 75 mM Tris-HCl (pH 6.8), 3.8% SDS, 4 M urea, and 20% glycerol. For western blot analyses of HEK293T cells, transfected cells were lysed in RIPA buffer supplemented with protease inhibitors. Protein concentrations were determined using the Pierce BCA protein assay kit (Thermo Fisher Scientific) according to the manufacturer's instructions. Lysates were resolved by SDS-PAGE and transferred to Immobilon-P PVDF membranes (Millipore). Membranes were blocked for 30 min at room temperature in Tris-buffered saline containing 0.5% Tween 20 (TBST) and 5% nonfat milk, followed by overnight incubation at 4°C with primary antibodies diluted in TBST containing 5% bovine serum albumin (BSA; Equitech-Bio, Inc.) and 0.05% NaN_3. Membranes were then incubated for 1 h at room temperature with horseradish peroxidase (HRP)-conjugated secondary antibodies diluted in blocking buffer. The following primary antibodies were used: anti-OPHN1 antibody (rabbit pAb, 1724, 1:500) (Govek et al. 2004), anti-MYC (mouse mAb IgG1 9E10, 1:500; BioLegend 626802), anti-FLAG (mouse mAb IgG1 [M2], 1:500; Sigma-Aldrich F3165), anti-GFP (mouse mAb IgG2a, 1:500; NeuroMab N86/8), anti-γ-tubulin (mouse mAb IgG1, 1:5000; Sigma GTU-88), and anti-vinculin (mouse mAb IgG2, 1:5000; R&D Systems MAB6896).

Statistical analysis

All data analyzed with parametrical tests are presented as mean ± SEM, while data analyzed with nonparametrical tests are presented as median (interquartile range). Statistical analyses were performed using GraphPad Prism 11 or Microsoft Excel. For fixed-tissue quantifications, each brain was considered a biological replicate. For live-imaging experiments, cells were pooled from independent IUEs, and the numbers of cells and independent experiments are reported in the corresponding figure legends. Comparisons between two groups were performed using unpaired, two-tailed Student's *t*-tests or Mann–Whitney *U*-test. Comparisons among more than two groups were performed using one-way analysis of variance (ANOVA) followed by Dunnett's or Tukey–Kramer post hoc multiple-comparison tests or the Kruskal–Wallis test followed by Dunn's post hoc test. Statistical significance was defined as follows: $P < 0.05$ (*), $P < 0.01$ (**), and $P < 0.001$ (***). *P*-values ≥0.05 were considered not significant.

Competing interest statement

The authors declare no competing interests.

Downloaded from on November 2, 2026 - Published by Cold Spring Harbor Laboratory Press

Acknowledgments

We thank Dr. Julian Nüchel, Dr. Rick Cerione, Dr. Franck Polleux, and Dr. Songhai Shi for providing plasmid constructs. We are grateful to Dr. Marcus Plomann for providing *Pacsin2* constructs and honor his memory and contributions to the field. We thank Dr. Pierre Billuart for his critical reading of the manuscript and valuable comments and suggestions. We also thank Ishana Chadha, Emily Krasnow, Gina Rizzo, Connor Fitzpatrick, Robert Harutyunyan, Katherine Matho, and members of the Van Aelst laboratory for technical assistance and/or helpful discussions. This work was supported by grants from the National Institutes of Health (R01NS116897 and R01MH119819) to L.V.A., and from the Canadian Institute of Health Research (PJT-153065) to J.-F.C. S.N. was supported by a doctoral award from the Fonds de Recherche du Québec-Santé. J.-F.C. holds the Canada Research Chair (Tier-1) in Cellular Signaling and Cancer Metastasis.

Author contributions: L.V.A. conceptualized the project. F.B., S.G., B.d.l.C.T., Y.-T.Y., C.-L.W., and S.N. performed experiments. F.B. performed data and statistical analyses. F.B., with the assistance of B.d.l.C.T., prepared the figures and movies. J.-F.C. supervised the BioID experiments. J.A.J. assisted with the BioID data analysis. L.V.A. wrote the manuscript, F.B. prepared the figure legends and the Materials and Methods, and all authors contributed to editing the manuscript.

References

Allegra M, Spalletti C, Vignoli B, Azzimondi S, Busti I, Billuart P, Canossa M, Caleo M. 2017. Pharmacological rescue of adult hippocampal neurogenesis in a mouse model of X-linked intellectual disability. *Neurobiol Dis* **100:** 75–86. doi:10.1016/j.nbd.2017.01.003

Amano M, Ito M, Kimura K, Fukata Y, Chihara K, Nakano T, Matsuura Y, Kaibuchi K. 1996. Phosphorylation and activation of myosin by Rho-associated kinase (Rho-kinase). *J Biol Chem* **271:** 20246–20249. doi:10.1074/jbc.271.34.20246

Amano M, Fukata Y, Kaibuchi K. 2000. Regulation and functions of Rho-associated kinase. *Exp Cell Res* **261:** 44–51. doi:10.1006/excr.2000.5046

Ayala R, Shu T, Tsai LH. 2007. Trekking across the brain: the journey of neuronal migration. *Cell* **128:** 29–43. doi:10.1016/j.cell.2006.12.021

Azzarelli R, Kerloch T, Pacary E. 2014. Regulation of cerebral cortex development by Rho GTPases: insights from in vivo studies. *Front Cell Neurosci* **8:** 445. doi:10.3389/fncel.2014.00445

Bagci H, Sriskandarajah N, Robert A, Boulais J, Elkholi IE, Tran V, Lin ZY, Thibault MP, Dubé N, Faubert D, et al. 2020. Mapping the proximity interaction network of the Rho-family GTPases reveals signalling pathways and regulatory mechanisms. *Nat Cell Biol* **22:** 120–134. doi:10.1038/s41556-019-0438-7

Bergmann C, Zerres K, Senderek J, Rudnik-Schoneborn S, Eggermann T, Hausler M, Mull M, Ramaekers VT. 2003. Oligophrenin 1 (OPHN1) gene mutation causes syndromic X-linked mental retardation with epilepsy, rostral ventricular enlargement and cerebellar hypoplasia. *Brain* **126:** 1537–1544. doi:10.1093/brain/awg173

Billuart P, Bienvenu T, Ronce N, des Portes V, Vinet MC, Zemni R, Roest Crollius H, Carrié A, Fauchereau F, Cherry M, et al. 1998. Oligophrenin-1 encodes a rhoGAP protein involved in X-linked mental retardation. *Nature* **392:** 923–926. doi:10.1038/31940

Biswas A, Whitehead MT, Haldipur P, Blaser S, Gowda VK, De Vita E, Josifova D, Jewell R, Menzies L, Mankad K, et al. 2026. Comprehensive structural MRI phenotyping in *Oligophrenin 1*-related disorder reveals characteristic brain malformations. *AJNR Am J Neuroradiol* **47:** 1946–1952. doi:10.3174/ajnr.A9184

Blum M, Andreeva A, Florentino LC, Chuguransky SR, Grego T, Hobbs E, Pinto BL, Orr A, Paysan-Lafosse T, Ponamareva I, et al. 2025. InterPro: the protein sequence classification resource in 2025. *Nucleic Acids Res* **53:** D444–D456. doi:10.1093/nar/gkae1082

Braun A, Pinyol R, Dahlhaus R, Koch D, Fonarev P, Grant BD, Kessels MM, Qualmann B. 2005. EHD proteins associate with syndapin I and II and such interactions play a crucial role in endosomal recycling. *Mol Biol Cell* **16:** 3642–3658. doi:10.1091/mbc.e05-01-0076

Bultje RS, Castaneda-Castellanos DR, Jan LY, Jan YN, Kriegstein AR, Shi SH. 2009. Mammalian Par3 regulates progenitor cell asymmetric division via notch signaling in the developing neocortex. *Neuron* **63:** 189–202. doi:10.1016/j.neuron.2009.07.004

Cappello S, Böhringer CR, Bergami M, Conzelmann KK, Ghanem A, Tomassy GS, Arlotta P, Mainardi M, Allegra M, Caleo M, et al. 2012. A radial glia-specific role of RhoA in double cortex formation. *Neuron* **73:** 911–924. doi:10.1016/j.neuron.2011.12.030

Casanova MF, Trippe J II. 2006. Regulatory mechanisms of cortical laminar development. *Brain Res Rev* **51:** 72–84. doi:10.1016/j.brainresrev.2005.10.002

Chabrol B, Girard N, N'Guyen K, Gérard A, Carlier M, Villard L, Philip N. 2005. Delineation of the clinical phenotype associated with *OPHN1* mutations based on the clinical and neuropsychological evaluation of three families. *Am J Med Genet A* **138:** 314–317. doi:10.1002/ajmg.a.30882

Compagnucci C, Barresi S, Petrini S, Billuart P, Piccini G, Chiurazzi P, Alfieri P, Bertini E, Zanni G. 2016. Rho kinase inhibition is essential during in vitro neurogenesis and promotes phenotypic rescue of human induced pluripotent stem cell-derived neurons with oligophrenin-1 loss of function. *Stem Cells Transl Med* **5:** 860–869. doi:10.5966/sctm.2015-0303

Cooper JA. 2013. Cell biology in neuroscience: mechanisms of cell migration in the nervous system. *J Cell Biol* **202:** 725–734. doi:10.1083/jcb.201305021

Corbetta S, Gualdoni S, Ciceri G, Monari M, Zuccaro E, Tybulewicz VL, de Curtis I. 2009. Essential role of Rac1 and Rac3 GTPases in neuronal development. *FASEB J* **23:** 1347–1357. doi:10.1096/fj.08-121574

Creppe C, Malinouskaya L, Volvert ML, Gillard M, Close P, Malaise O, Laguesse S, Cornez I, Rahmouni S, Ormenese S, et al. 2009. Elongator controls the migration and differentiation of cortical neurons through acetylation of α-tubulin. *Cell* **136:** 551–564. doi:10.1016/j.cell.2008.11.043

Cresto N, Lebrun N, Dumont F, Letourneur F, Billuart P, Rouach N. 2022. Hippocampal excitatory synaptic transmission and plasticity are differentially altered during postnatal development by loss of the X-linked intellectual disability protein oligophrenin-1. *Cells* **11:** 1545. doi:10.3390/cells11091545

de Kreuk BJ, Nethe M, Fernandez-Borja M, Anthony EC, Hensbergen PJ, Deelder AM, Plomann M, Hordijk PL. 2011. The F-BAR domain protein PACSIN2 associates with Rac1 and

Downloaded from on November 2, 2026 - Published by Cold Spring Harbor Laboratory Press

regulates cell spreading and migration. *J Cell Sci* **124:** 2375–2388. doi:10.1242/jcs.080630

des Portes V, Boddaert N, Sacco S, Briault S, Maincent K, Bahi N, Gomot M, Ronce N, Bursztyn J, Adamsbaum C, et al. 2004. Specific clinical and brain MRI features in mentally retarded patients with mutations in the oligophrenin-1 gene. *Am J Med Genet A* **124A:** 364–371. doi:10.1002/ajmg.a.20422

Deuel TA, Liu JS, Corbo JC, Yoo SY, Rorke-Adams LB, Walsh CA. 2006. Genetic interactions between doublecortin and doublecortin-like kinase in neuronal migration and axon outgrowth. *Neuron* **49:** 41–53. doi:10.1016/j.neuron.2005.10.038

Dorland YL, Malinova TS, van Stalborch AM, Grieve AG, van Geemen D, Jansen NS, de Kreuk BJ, Nawaz K, Kole J, Geerts D, et al. 2016. The F-BAR protein pacsin2 inhibits asymmetric VE-cadherin internalization from tensile adherens junctions. *Nat Commun* **7:** 12210. doi:10.1038/ncomms12210

Dumont V, Lehtonen S. 2022. PACSIN proteins in vivo: roles in development and physiology. *Acta Physiol (Oxf)* **234:** e13783. doi:10.1111/apha.13783

Dupraz S, Hilton BJ, Husch A, Santos TE, Coles CH, Stern S, Brakebusch C, Bradke F. 2019. RhoA controls axon extension independent of specification in the developing brain. *Curr Biol* **29:** 3874–3886.e9. doi:10.1016/j.cub.2019.09.040

Fernández V, Llinares-Benadero C, Borrell V. 2016. Cerebral cortex expansion and folding: what have we learned? *EMBO J* **35:** 1021–1044. doi:10.15252/embj.201593701

Francis F, Cappello S. 2021. Neuronal migration and disorders - an update. *Curr Opin Neurobiol* **66:** 57–68. doi:10.1016/j.conb.2020.10.002

Gleeson JG, Lin PT, Flanagan LA, Walsh CA. 1999. Doublecortin is a microtubule-associated protein and is expressed widely by migrating neurons. *Neuron* **23:** 257–271. doi:10.1016/S0896-6273(00)80778-3

Godin JD, Thomas N, Laguesse S, Malinouskaya L, Close P, Malaise O, Purnelle A, Raineteau O, Campbell K, Fero M, et al. 2012. p27(Kip1) is a microtubule-associated protein that promotes microtubule polymerization during neuron migration. *Dev Cell* **23:** 729–744. doi:10.1016/j.devcel.2012.08.006

Govek EE, Newey SE, Akerman CJ, Cross JR, Van der Veken L, Van Aelst L. 2004. The X-linked mental retardation protein oligophrenin-1 is required for dendritic spine morphogenesis. *Nat Neurosci* **7:** 364–372. doi:10.1038/nn1210

Govek EE, Newey SE, Van Aelst L. 2005. The role of the Rho GTPases in neuronal development. *Genes Dev* **19:** 1–49. doi:10.1101/gad.1256405

Govek EE, Hatten ME, Van Aelst L. 2011. The role of Rho GTPase proteins in CNS neuronal migration. *Dev Neurobiol* **71:** 528–553. doi:10.1002/dneu.20850

Greig LC, Woodworth MB, Galazo MJ, Padmanabhan H, Macklis JD. 2013. Molecular logic of neocortical projection neuron specification, development and diversity. *Nat Rev Neurosci* **14:** 755–769. doi:10.1038/nrn3586

Grimm-Gunter EM, Milbrandt M, Merkl B, Paulsson M, Plomann M. 2008. PACSIN proteins bind tubulin and promote microtubule assembly. *Exp Cell Res* **314:** 1991–2003. doi:10.1016/j.yexcr.2008.03.015

Hansen AH, Hippenmeyer S. 2020. Non-cell-autonomous mechanisms in radial projection neuron migration in the developing cerebral cortex. *Front Cell Dev Biol* **8:** 574382. doi:10.3389/fcell.2020.574382

Heng JI, Chariot A, Nguyen L. 2010. Molecular layers underlying cytoskeletal remodelling during cortical development. *Trends Neurosci* **33:** 38–47. doi:10.1016/j.tins.2009.09.003

Insolera R, Shao W, Airik R, Hildebrandt F, Shi SH. 2014. SDCCAG8 regulates pericentriolar material recruitment and neuronal migration in the developing cortex. *Neuron* **83:** 805–822. doi:10.1016/j.neuron.2014.06.029

Jabaudon D. 2017. Fate and freedom in developing neocortical circuits. *Nat Commun* **8:** 16042. doi:10.1038/ncomms16042

Jossin Y, Cooper JA. 2011. Reelin, Rap1 and N-cadherin orient the migration of multipolar neurons in the developing neocortex. *Nat Neurosci* **14:** 697–703. doi:10.1038/nn.2816

Kawa AB, Hwang EK, Funke JR, Zhou H, Costa-Mattioli M, Wolf ME. 2022. Positive allosteric modulation of mGlu(1) reverses cocaine-induced behavioral and synaptic plasticity through the integrated stress response and oligophrenin-1. *Biol Psychiatry* **92:** 871–879. doi:10.1016/j.biopsych.2022.05.008

Kawauchi T. 2011. Regulation of cell adhesion and migration in cortical neurons: not only Rho but also Rab family small GTPases. *Small GTPases* **2:** 36–40. doi:10.4161/sgtp.2.1.15001

Kawauchi T, Chihama K, Nabeshima Y, Hoshino M. 2006. Cdk5 phosphorylates and stabilizes p27kip1 contributing to actin organization and cortical neuronal migration. *Nat Cell Biol* **8:** 17–26. doi:10.1038/ncb1338

Kessels MM, Qualmann B. 2006. Syndapin oligomers interconnect the machineries for endocytic vesicle formation and actin polymerization. *J Biol Chem* **281:** 13285–13299. doi:10.1074/jbc.M510226200

Khelfaoui M, Denis C, van Galen E, de Bock F, Schmitt A, Houbron C, Morice E, Giros B, Ramakers G, Fagni L, et al. 2007. Loss of X-linked mental retardation gene oligophrenin1 in mice impairs spatial memory and leads to ventricular enlargement and dendritic spine immaturity. *J Neurosci* **27:** 9439–9450. doi:10.1523/JNEUROSCI.2029-07.2007

Khelfaoui M, Pavlowsky A, Powell AD, Valnegri P, Cheong KW, Blandin Y, Passafaro M, Jefferys JG, Chelly J, Billuart P. 2009. Inhibition of RhoA pathway rescues the endocytosis defects in oligophrenin1 mouse model of mental retardation. *Hum Mol Genet* **18:** 2575–2583. doi:10.1093/hmg/ddp189

Khelfaoui M, Gambino F, Houbaert X, Ragazzon B, Müller C, Carta M, Lanore F, Srikumar BN, Gastrein P, Lepleux M, et al. 2014. Lack of the presynaptic RhoGAP protein oligophrenin1 leads to cognitive disabilities through dysregulation of the cAMP/PKA signalling pathway. *Philos Trans R Soc Lond B Biol Sci* **369:** 20130160. doi:10.1098/rstb.2013.0160

Kimura K, Ito M, Amano M, Chihara K, Fukata Y, Nakafuku M, Yamamori B, Feng J, Nakano T, Okawa K, et al. 1996. Regulation of myosin phosphatase by Rho and Rho-associated kinase (Rho-kinase). *Science* **273:** 245–248. doi:10.1126/science.273.5272.245

Koch JC, Tönges L, Michel U, Bähr M, Lingor P. 2014. Viral vector-mediated downregulation of RhoA increases survival and axonal regeneration of retinal ganglion cells. *Front Cell Neurosci* **8:** 273. doi:10.3389/fncel.2014.00273

Kriegstein AR, Noctor SC. 2004. Patterns of neuronal migration in the embryonic cortex. *Trends Neurosci* **27:** 392–399. doi:10.1016/j.tins.2004.05.001

Liaci C, Camera M, Caslini G, Rando S, Contino S, Romano V, Merlo GR. 2021. Neuronal cytoskeleton in intellectual disability: from systems biology and modeling to therapeutic opportunities. *Int J Mol Sci* **22:** 6167. doi:10.3390/ijms22116167

Lian G, Sheen VL. 2015. Cytoskeletal proteins in cortical development and disease: actin associated proteins in periventricular heterotopia. *Front Cell Neurosci* **9:** 99. doi:10.3389/fncel.2015.00099

Malatesta P, Götz M. 2013. Radial glia—from boring cables to stem cell stars. *Development* **140:** 483–486. doi:10.1242/dev.085852

Downloaded from on November 2, 2026 - Published by Cold Spring Harbor Laboratory Press

Malatesta P, Hartfuss E, Götz M. 2000. Isolation of radial glial cells by fluorescent-activated cell sorting reveals a neuronal lineage. *Development* **127:** 5253–5263. doi:10.1242/dev.127.24.5253

Marin O, Rubenstein JL. 2003. Cell migration in the forebrain. *Annu Rev Neurosci* **26:** 441–483. doi:10.1146/annurev.neuro.26.041002.131058

Métin C, Vallee RB, Rakic P, Bhide PG. 2008. Modes and mishaps of neuronal migration in the mammalian brain. *J Neurosci* **28:** 11746–11752. doi:10.1523/JNEUROSCI.3860-08.2008

Miyata T, Kawaguchi A, Okano H, Ogawa M. 2001. Asymmetric inheritance of radial glial fibers by cortical neurons. *Neuron* **31:** 727–741. doi:10.1016/S0896-6273(01)00420-2

Modregger J, Ritter B, Witter B, Paulsson M, Plomann M. 2000. All three PACSIN isoforms bind to endocytic proteins and inhibit endocytosis. *J Cell Sci* **113:** 4511–4521. doi:10.1242/jcs.113.24.4511

Molyneaux BJ, Arlotta P, Menezes JR, Macklis JD. 2007. Neuronal subtype specification in the cerebral cortex. *Nat Rev Neurosci* **8:** 427–437. doi:10.1038/nrn2151

Moon HM, Wynshaw-Boris A. 2013. Cytoskeleton in action: lissencephaly, a neuronal migration disorder. *Wiley Interdiscip Rev Dev Biol* **2:** 229–245. doi:10.1002/wdev.67

Moortgat S, Lederer D, Deprez M, Buzatu M, Clapuyt P, Boulanger S, Benoit V, Mary S, Guichet A, Ziegler A, et al. 2018. Expanding the phenotypic spectrum associated with OPHN1 mutations: report of 17 individuals with intellectual disability but no cerebellar hypoplasia. *Eur J Med Genet* **61:** 442–450. doi:10.1016/j.ejmg.2018.03.002

Nadarajah B, Brunstrom JE, Grutzendler J, Wong RO, Pearlman AL. 2001. Two modes of radial migration in early development of the cerebral cortex. *Nat Neurosci* **4:** 143–150. doi:10.1038/83967

Nadif Kasri N, Nakano-Kobayashi A, Malinow R, Li B, Van Aelst L. 2009. The Rho-linked mental retardation protein oligophrenin-1 controls synapse maturation and plasticity by stabilizing AMPA receptors. *Genes Dev* **23:** 1289–1302. doi:10.1101/gad.1783809

Nadif Kasri N, Nakano-Kobayashi A, Van Aelst L. 2011. Rapid synthesis of the X-linked mental retardation protein OPHN1 mediates mGluR-dependent LTD through interaction with the endocytic machinery. *Neuron* **72:** 300–315. doi:10.1016/j.neuron.2011.09.001

Nahlé S, Quirion L, Boulais J, Bagci H, Faubert D, Gingras AC, Côté JF. 2022. Defining the interactomes of proteins involved in cytoskeletal dynamics using high-throughput proximity-dependent biotinylation in cellulo. *STAR Protoc* **3:** 101075. doi:10.1016/j.xpro.2021.101075

Nakano-Kobayashi A, Kasri NN, Newey SE, Van Aelst L. 2009. The Rho-linked mental retardation protein OPHN1 controls synaptic vesicle endocytosis via endophilin A1. *Curr Biol* **19:** 1133–1139. doi:10.1016/j.cub.2009.05.022

Nakano-Kobayashi A, Tai Y, Nadif Kasri N, Van Aelst L. 2014. The X-linked mental retardation protein OPHN1 interacts with Homer1b/c to control spine endocytic zone positioning and expression of synaptic potentiation. *J Neurosci* **34:** 8665–8671. doi:10.1523/JNEUROSCI.0894-14.2014

Nguyen L, Besson A, Heng JI, Schuurmans C, Teboul L, Parras C, Philpott A, Roberts JM, Guillemot F. 2006. P27kip1 independently promotes neuronal differentiation and migration in the cerebral cortex. *Genes Dev* **20:** 1511–1524. doi:10.1101/gad.377106

Noctor SC, Flint AC, Weissman TA, Dammerman RS, Kriegstein AR. 2001. Neurons derived from radial glial cells establish radial units in neocortex. *Nature* **409:** 714–720. doi:10.1038/35055553

Noctor SC, Martínez-Cerdeño V, Ivic L, Kriegstein AR. 2004. Cortical neurons arise in symmetric and asymmetric division zones and migrate through specific phases. *Nat Neurosci* **7:** 136–144. doi:10.1038/nn1172

Pacary E, Heng J, Azzarelli R, Riou P, Castro D, Lebel-Potter M, Parras C, Bell DM, Ridley AJ, Parsons M, et al. 2011. Proneural transcription factors regulate different steps of cortical neuron migration through Rnd-mediated inhibition of RhoA signaling. *Neuron* **69:** 1069–1084. doi:10.1016/j.neuron.2011.02.018

Paysan-Lafosse T, Andreeva A, Blum M, Chuguransky SR, Grego T, Pinto BL, Salazar GA, Bileschi ML, Llinares-Lopez F, Meng-Papaxanthos L, et al. 2025. The Pfam protein families database: embracing AI/ML. *Nucleic Acids Res* **53:** D523–D534. doi:10.1093/nar/gkae997

Philip N, Chabrol B, Lossi AM, Cardoso C, Guerrini R, Dobyns WB, Raybaud C, Villard L. 2003. Mutations in the oligophrenin-1 gene (*OPHN1*) cause X linked congenital cerebellar hypoplasia. *J Med Genet* **40:** 441–446. doi:10.1136/jmg.40.6.441

Pirozzi F, Di Raimo FR, Zanni G, Bertini E, Billuart P, Tartaglione T, Tabolacci E, Brancaccio A, Neri G, Chiurazzi P. 2011. Insertion of 16 amino acids in the BAR domain of the oligophrenin 1 protein causes mental retardation and cerebellar hypoplasia in an Italian family. *Hum Mutat* **32:** E2294–E2307. doi:10.1002/humu.21567

Powell AD, Gill KK, Saintot PP, Jiruska P, Chelly J, Billuart P, Jefferys JG. 2012. Rapid reversal of impaired inhibitory and excitatory transmission but not spine dysgenesis in a mouse model of mental retardation. *J Physiol* **590:** 763–776. doi:10.1113/jphysiol.2011.219907

Qualmann B, Kelly RB. 2000. Syndapin isoforms participate in receptor-mediated endocytosis and actin organization. *J Cell Biol* **148:** 1047–1062. doi:10.1083/jcb.148.5.1047

Quan A, Robinson PJ. 2013. Syndapin--a membrane remodelling and endocytic F-BAR protein. *FEBS J* **280:** 5198–5212. doi:10.1111/febs.12343

Redolfi N, Galla L, Maset A, Murru L, Savoia E, Zamparo I, Gritti A, Billuart P, Passafaro M, Lodovichi C. 2016. Oligophrenin-1 regulates number, morphology and synaptic properties of adult-born inhibitory interneurons in the olfactory bulb. *Hum Mol Genet* **25:** 5198–5211. doi:10.1093/hmg/ddw340

Riento K, Ridley AJ. 2003. Rocks: multifunctional kinases in cell behaviour. *Nat Rev Mol Cell Biol* **4:** 446–456. doi:10.1038/nrm1128

Ross ME, Walsh CA. 2001. Human brain malformations and their lessons for neuronal migration. *Annu Rev Neurosci* **24:** 1041–1070. doi:10.1146/annurev.neuro.24.1.1041

Roux KJ, Kim DI, Raida M, Burke B. 2012. A promiscuous biotin ligase fusion protein identifies proximal and interacting proteins in mammalian cells. *J Cell Biol* **196:** 801–810. doi:10.1083/jcb.201112098

Santos-Rebouças CB, Belet S, Guedes de Almeida L, Ribeiro MG, Medina-Acosta E, Bahia PR, Alves da Silva AF, Lima dos Santos F, Borges de Lacerda GC, Pimentel MM, et al. 2014. A novel in-frame deletion affecting the BAR domain of OPHN1 in a family with intellectual disability and hippocampal alterations. *Eur J Hum Genet* **22:** 644–651. doi:10.1038/ejhg.2013.216

Schwartz TS, Wojcik MH, Pelletier RC, Edward HL, Picker JD, Holm IA, Towne MC, Beggs AH, Agrawal PB. 2019. Expanding the phenotypic spectrum associated with OPHN1 variants. *Eur J Med Genet* **62:** 137–143. doi:10.1016/j.ejmg.2018.06.015

Downloaded from on November 2, 2026 - Published by Cold Spring Harbor Laboratory Press

Senju Y, Itoh Y, Takano K, Hamada S, Suetsugu S. 2011. Essential role of PACSIN2/syndapin-II in caveolae membrane sculpting. *J Cell Sci* **124:** 2032–2040. doi:10.1242/jcs.086264

Shikanai M, Nakajima K, Kawauchi T. 2011. N-cadherin regulates radial glial fiber-dependent migration of cortical locomoting neurons. *Commun Integr Biol* **4:** 326–330. doi:10.4161/cib.4.3.14886

Silva CG, Peyre E, Nguyen L. 2019. Cell migration promotes dynamic cellular interactions to control cerebral cortex morphogenesis. *Nat Rev Neurosci* **20:** 318–329. doi:10.1038/s41583-019-0148-y

Snider CE, Wan Mohamad Noor WNI, Nguyen NTH, Gould KL, Suetsugu S. 2021. The state of F-BAR domains as membrane-bound oligomeric platforms. *Trends Cell Biol* **31:** 644–655. doi:10.1016/j.tcb.2021.03.013

Solecki DJ, Govek EE, Tomoda T, Hatten ME. 2006. Neuronal polarity in CNS development. *Genes Dev* **20:** 2639–2647. doi:10.1101/gad.1462506

Stouffer MA, Golden JA, Francis F. 2016. Neuronal migration disorders: focus on the cytoskeleton and epilepsy. *Neurobiol Dis* **92:** 18–45. doi:10.1016/j.nbd.2015.08.003

Tabata H, Nakajima K. 2003. Multipolar migration: the third mode of radial neuronal migration in the developing cerebral cortex. *J Neurosci* **23:** 9996–10001. doi:10.1523/JNEUROSCI.23-31-09996.2003

Tang J, Ip JP, Ye T, Ng YP, Yung WH, Wu Z, Fang W, Fu AK, Ip NY. 2014. Cdk5-dependent Mst3 phosphorylation and activity regulate neuronal migration through RhoA inhibition. *J Neurosci* **34:** 7425–7436. doi:10.1523/JNEUROSCI.5449-13.2014

Taverna E, Götz M, Huttner WB. 2014. The cell biology of neurogenesis: toward an understanding of the development and evolution of the neocortex. *Annu Rev Cell Dev Biol* **30:** 465–502. doi:10.1146/annurev-cellbio-101011-155801

Tentler D, Gustavsson P, Leisti J, Schueler M, Chelly J, Timonen E, Anneren G, Willard HF, Dahl N. 1999. Deletion including the oligophrenin-1 gene associated with enlarged cerebral ventricles, cerebellar hypoplasia, seizures and ataxia. *Eur J Hum Genet* **7:** 541–548. doi:10.1038/sj.ejhg.5200320

Teo G, Liu G, Zhang J, Nesvizhskii AI, Gingras AC, Choi H. 2014. SAINTexpress: improvements and additional features in Significance Analysis of INTeractome software. *J Proteomics* **100:** 37–43. doi:10.1016/j.jprot.2013.10.023

Uehata M, Ishizaki T, Satoh H, Ono T, Kawahara T, Morishita T, Tamakawa H, Yamagami K, Inui J, Maekawa M, et al. 1997. Calcium sensitization of smooth muscle mediated by a Rho-associated protein kinase in hypertension. *Nature* **389:** 990–994. doi:10.1038/40187

Vaid S, Huttner WB. 2022. Progenitor-based cell biological aspects of neocortex development and evolution. *Front Cell Dev Biol* **10:** 892922. doi:10.3389/fcell.2022.892922

Valiente M, Marín O. 2010. Neuronal migration mechanisms in development and disease. *Curr Opin Neurobiol* **20:** 68–78. doi:10.1016/j.conb.2009.12.003

Wang Q, Navarro MV, Peng G, Molinelli E, Goh SL, Judson BL, Rajashankar KR, Sondermann H. 2009. Molecular mechanism of membrane constriction and tubulation mediated by the F-BAR protein Pacsin/Syndapin. *Proc Natl Acad Sci* **106:** 12700–12705. doi:10.1073/pnas.0902974106

Wang M, Gallo NB, Tai Y, Li B, Van Aelst L. 2021. Oligophrenin-1 moderates behavioral responses to stress by regulating parvalbumin interneuron activity in the medial prefrontal cortex. *Neuron* **109:** 1636–1656.e8. doi:10.1016/j.neuron.2021.03.016

Wegiel J, Kuchna I, Nowicki K, Imaki H, Wegiel J, Marchi E, Ma SY, Chauhan A, Chauhan V, Bobrowicz TW, et al. 2010. The neuropathology of autism: defects of neurogenesis and neuronal migration, and dysplastic changes. *Acta Neuropathol* **119:** 755–770. doi:10.1007/s00401-010-0655-4

Wu Q, Liu J, Fang A, Li R, Bai Y, Kriegstein AR, Wang X. 2014. The dynamics of neuronal migration. *Adv Exp Med Biol* **800:** 25–36. doi:10.1007/978-94-007-7687-6_2

Xu Z, Chen Y, Chen Y. 2019. Spatiotemporal regulation of Rho GTPases in neuronal migration. *Cells* **8:** 568. doi:10.3390/cells8060568

Yang YT, Wang CL, Van Aelst L. 2012. DOCK7 interacts with TACC3 to regulate interkinetic nuclear migration and cortical neurogenesis. *Nat Neurosci* **15:** 1201–1210. doi:10.1038/nn.3171

Zanni G, Saillour Y, Nagara M, Billuart P, Castelnau L, Moraine C, Faivre L, Bertini E, Durr A, Guichet A, et al. 2005. Oligophrenin 1 mutations frequently cause X-linked mental retardation with cerebellar hypoplasia. *Neurology* **65:** 1364–1369. doi:10.1212/01.wnl.0000182813.94713.ee

Zhang CL, Aime M, Laheranne E, Houbaert X, El Oussini H, Martin C, Lepleux M, Normand E, Chelly J, Herzog E, et al. 2017. Protein kinase A deregulation in the medial prefrontal cortex impairs working memory in murine oligophrenin-1 deficiency. *J Neurosci* **37:** 11114–11126. doi:10.1523/JNEUROSCI.0351-17.2017

Downloaded from on November 2, 2026 - Published by Cold Spring Harbor Laboratory Press



Distinct domains of Oligophrenin-1 regulate successive phases of cortical radial migration via RHOA- and PACSIN2-dependent mechanisms

Francesco Boato, Benjamin de la Cruz Thea, Shanu George, et al.

Genes Dev. published online October 29, 2026
Access the most recent version at doi:10.1101/gad.354125.126

Supplemental Material https://genesdev.cshlp.org/content/suppl/2026/10/29/gad.354125.126.DC1

Published online October 29, 2026 in advance of the full issue.

Creative Commons License This article, published in *Genes & Development*, is available under a Creative Commons License (Attribution-NonCommercial 4.0 International), as described at http://creativecommons.org/licenses/by-nc/4.0/.

Email Alerting Service Receive free email alerts when new articles cite this article - sign up in the box at the top right corner of the article or **click here.**



Published by © 2026 Boato et al.; Published by Cold Spring Harbor Laboratory Press